



## RESEARCH ARTICLE

10.1002/2017JB014892

## Key Points:

- Full coupling between the fluid and the solid in arbitrarily fractured porous media
- Fractures introduce a separate set of fluid and solid constitutive laws and add nonlinearity
- A complete computational model including a hybrid-dimensional two-field mixed finite element method for efficient space discretization

## Correspondence to:

L. Jin,  
leijin@stanford.edu

## Citation:

Jin, L., & Zoback, M. D. (2017). Fully coupled nonlinear fluid flow and poroelasticity in arbitrarily fractured porous media: A hybrid-dimensional computational model. *Journal of Geophysical Research: Solid Earth*, 122, 7626–7658. <https://doi.org/10.1002/2017JB014892>

Received 21 AUG 2017

Accepted 26 AUG 2017

Accepted article online 30 AUG 2017

Published online 21 OCT 2017

©2017. The Authors.

This is an open access article under the terms of the Creative Commons Attribution-NonCommercial-NoDerivs License, which permits use and distribution in any medium, provided the original work is properly cited, the use is non-commercial and no modifications or adaptations are made.

## Fully Coupled Nonlinear Fluid Flow and Poroelasticity in Arbitrarily Fractured Porous Media: A Hybrid-Dimensional Computational Model

L. Jin<sup>1</sup> and M. D. Zoback<sup>1</sup>

<sup>1</sup>Department of Geophysics, Stanford University, Stanford, CA, USA

**Abstract** We formulate the problem of fully coupled transient fluid flow and quasi-static poroelasticity in arbitrarily fractured, deformable porous media saturated with a single-phase compressible fluid. The fractures we consider are hydraulically highly conductive, allowing discontinuous fluid flux across them; mechanically, they act as finite-thickness shear deformation zones prior to failure (i.e., nonslipping and nonpropagating), leading to “apparent discontinuity” in strain and stress across them. Local nonlinearity arising from pressure-dependent permeability of fractures is also included. Taking advantage of typically high aspect ratio of a fracture, we do not resolve transversal variations and instead assume uniform flow velocity and simple shear strain within each fracture, rendering the coupled problem numerically more tractable. Fractures are discretized as lower dimensional zero-thickness elements tangentially conforming to unstructured matrix elements. A hybrid-dimensional, equal-low-order, two-field mixed finite element method is developed, which is free from stability issues for a drained coupled system. The fully implicit backward Euler scheme is employed for advancing the fully coupled solution in time, and the Newton-Raphson scheme is implemented for linearization. We show that the fully discretized system retains a canonical form of a fracture-free poromechanical problem; the effect of fractures is translated to the modification of some existing terms as well as the addition of several terms to the capacity, conductivity, and stiffness matrices therefore allowing the development of independent subroutines for treating fractures within a standard computational framework. Our computational model provides more realistic inputs for some fracture-dominated poromechanical problems like fluid-induced seismicity.

### 1. Introduction

Coupled fluid pressure and solid stress occurring in geological media are important inputs for studying various geophysical and engineering problems, including induced seismicity associated with CO<sub>2</sub> sequestration or wastewater injection and stimulation of low-permeability hydrocarbon and geothermal reservoirs. A geological medium is often represented with a porous and linearly elastic solid infiltrated by fluid, referred to as the Biot poroelastic system (Biot, 1941). In terms of coupling, the Biot’s governing laws state that the pore pressure gradient acts as an equivalent body force that drives changes in deformation and stress, and the volumetric strain rate acts as an equivalent fluid source that drives changes in fluid pressure. Some classic analytical solutions have been derived for predicting poromechanical responses of the Biot system, provided appropriate geometric settings, boundary conditions, and material property distributions (e.g., Booker & Carter, 1986; Cleary, 1977; Rudnicki, 1986; Segall, 1985; Wang & Kümpel, 2003). For a more general Biot system, numerical solutions are also available. These solutions are obtained using various space discretization methods, including, for example, the mixed finite element method (e.g., Ferronato et al., 2010; Korsawe et al., 2006), the finite volume method (e.g., Nordbotten, 2014), and their combinations (e.g., Castelletto et al., 2015b), and they can be advanced in time in either a fully coupled manner or a proven stable sequentially coupled manner (e.g., Kim et al., 2011; White et al., 2016).

Often the geological medium is also embedded with a preexisting discrete fracture network (DFN). Including a DFN in the system introduces not only additional constitutive behaviors, either linear or nonlinear (Hu et al., 2017; Rutqvist & Stephansson, 2003), but also constraining and coupling on interfaces and intersections (e.g., Beavers & Joseph, 1967; Formaggia et al., 2014; Pouya, 2012). In addition, field variables and their gradients often become discontinuous across fractures, commonly referred to as “strong” and “weak” discontinuities (e.g., Borja, 2013; Hansbo & Hansbo, 2004). Specifically, for a fluid-solid coupled problem in which it is the fluid pressure and the solid displacement that are commonly selected

as the primary unknowns, we define a fracture as the following type of discontinuity based on a given scenario: (1) a *hydraulic strong discontinuity*, when the fracture is nonconductive and is embedded within a conductive matrix, and therefore, the pressure across it becomes discontinuous; (2) a *hydraulic weak discontinuity*, when the fracture is more conductive than the surrounding matrix, leading to discontinuous fluid flux across it; (3) a *mechanical strong discontinuity*, when the fracture opens or slides and the solid displacement is thus discontinuous; (4) a *mechanical weak discontinuity*, when the fracture behaves similar to a localized deformation band (i.e., shear band and compaction band), rendering the solid strain discontinuous.

Aside from the additional physics, the geometric complexity and the associated anisotropy and heterogeneity in material property also impose significant challenges on the modeling of a DFN-matrix system. To facilitate the setup of a mathematical model, a common representation is to define an equivalent continuum characterized by effective, homogenized, or upscaled parameters. For example, for the solid problem, an equivalent compliance or stiffness tensor based on analytical methods has been calculated for a few types of regularly fractured solid (Hudson & Liu, 1999; Liu et al., 2000). Similarly, for the fluid problem, a variety of models have been developed, including the classic dual-porosity double-permeability (DPDP) model (Barenblatt et al., 1960; Warren & Root, 1963). This model regularizes a fractured medium into a sugar-cube representation and calculates a shape factor, which can also be analytically based (Lim & Aziz, 1995); two sets of governing equations are formulated over the fracture domain and the matrix domain, respectively, and interact through mass exchange in response to the pressure gradient. This concept has been extended to triple-continuum (Wu et al., 2004) and multicontinuum models (Dietrich et al., 2005), with even multirate mass transfer (Tecklenburg et al., 2016). The major challenge for applying this family of models lies in the appropriate characterization of the DFN geometry. A remedy is to carry out the mass exchange in a computational domain rather than a physical domain, leading to a DPDP-reminiscent model without using shape factors (Lamb et al., 2013; Norbeck et al., 2015). On the other hand, some single-continuum models, which utilize flow-based upscaled hydraulic properties, provide an alternative that is less geometry-dependent (e.g., Berkowitz et al., 1988; Chen et al., 2015). An even simpler model is to smear the hydraulic properties of a fracture onto the background matrix according to certain geometry-based mapping rules (Lamb et al., 2013). In the above models, the original DFN is not resolved in a spatially explicit fashion. This drawback is overcome by an increasingly popular approach, namely, the discrete fracture-matrix model (Karimi-Fard et al., 2003; Sandve et al., 2012), which retains a given DFN and accounts for flow in both the matrix and fractures; thus, the model is physically more representative. This model can be reduced to a discrete fracture model, which is appropriate when the system is dominated by highly conductive fractures, or the porous matrix is nearly impermeable (e.g., Erhel et al., 2009; Hyman et al., 2015). The model can also be modified by using empirical (Unsal et al., 2010) or averaged (Sandve et al., 2014) matrix flow for beneficiary trade-off between accuracy and efficiency. Since fractures often occur at multiple length scales, the discrete fracture-matrix model becomes computationally demanding if all fractures are to be resolved. As a hybrid of the equivalent continuum model and the discrete fracture-matrix model, a family of multiscale and hierarchical models has been proposed, in which larger-scale fractures are explicitly represented through coarse meshing, whereas smaller-scale fractures are upscaled, and their coupling on the boundaries are enforced (Hou & Wu, 1997; Lee et al., 2001). For coupled poromechanical problems, it is important to explicitly represent at least those large-scale fractures, as they often can cause statistically significant variations (Berkowitz, 2002; Hardebol et al., 2015; Hirthe & Graf, 2015; Vujević et al., 2014), thus dominating the pressure field and the stress state within the domain and on fractures.

In terms of space discretization, explicit representation of fractures is associated with several issues. First, we must choose the fracture dimensionality. In the case of a small number of finite-thickness fractures, equal-dimensional representation of fractures and the matrix can be used (e.g., Gebauer et al., 2002; Geiger et al., 2004). This approach offers great convenience, as the same formulation can be used across the entire domain, but becomes impractical in the case of a large number of fractures. In addition, a fracture usually has a high aspect ratio, with its thickness orders of magnitude lower than its length and a typical mesh size of the matrix. Explicitly resolving fracture thickness through local fine meshing may lead to poorly conditioned discretization matrices and pose restrictions on certain time-stepping schemes. One alternative is to treat fractures as lower dimensional boundaries or entities conforming at fracture-matrix interfaces. For

example, within the framework of the finite element method, Juanes et al. (2002) proposed a hypersurface element technique for global-to-local mapping of the integration over lower dimensional fractures. A so-called interface element method has also been developed, which discretizes a zero-thickness fracture into double- or triple-layer nodes, and is designed specifically for hydraulic strong discontinuities (Cerfontaine et al., 2015; Segura & Carol, 2008a, 2008b). Sometimes a hybrid-dimensional representation also requires the averaging of conservation and constitutive laws across fractures (Martin et al., 2005). The second issue lies in mesh conformity, as is typically required by a hybrid-dimensional approach. In the case of a conductive fracture and hence continuous pressure across it, mesh conformity is desirable for convenience in enforcing pressure continuity, although a nonconforming mesh can also be used (Tunc et al., 2012). Conforming mesh generation can be a nontrivial problem in itself. For example, a Delaunay triangulation generally does not guarantee a high-quality fracture-conforming mesh, and recovery of the fracture geometry may lead to violation of certain important rules (Mustapha, 2014). Also, fractures displaying penalizing connection configurations can pose significant difficulties in meshing due to small angles and close points (Erhel et al., 2009). The third issue is that a complex DFN geometry generally requires unstructured discretization. Numerical solutions using the finite difference method or the finite volume method have been shown to be successful on unstructured grids (M. Karimi-Fard et al., 2003; Reichenberger et al., 2006). When coupled to solid mechanics problems, however, a common practice is to use the finite element method, which typically introduces a different set of mesh, to solve for the deformation, strain, and stress. The mapping of solutions between two sets of mesh can be computationally costly and lead to excessive numerical smearing and slow convergence (Sandve et al., 2014). All the above issues should be carefully addressed before proceeding to seek for numerical solutions.

The aforementioned studies investigate extensively either the fluid problem only in a fractured porous medium or the fluid-solid coupled poroelastic problem in a fracture-free porous medium. The challenges associated with fractures, as summarized above, render the fully coupled poroelastic model of arbitrarily fractured media difficult to build and the solution difficult to find. To our best knowledge, there seems no available analytical solution to a fully coupled poroelastic problem in a medium embedded even with a single fracture. Numerical solutions do exist. For example, by treating fractures as equal-dimensional entities, one can utilize existing tools to solve the fully coupled equations (e.g., Chang & Segall, 2016). This approach effectively models fractures as a “porous” domain similar to the surrounding medium and do not account for a separate fluid constitutive law within fractures. Other numerical solutions have been proposed which take into account the constitutive behavior of the fluid but not the solid within the fracture (Garipov et al., 2016; Vinci et al., 2014). Another solution based on a so-called “numerical manifold method” is obtained but requires simplification of a fracture network into a few dominant fractures (Hu et al., 2017). Finally, we also mention a class of model that pairs the classic DPDP model of the fluid with a modified solid model based on a so-called double effective stress law, and the numerical solution is obtained through an equal-dimensional finite element discretization (Elsworth & Bai, 1992; Gelet et al., 2012; Khalili & Selvadurai, 2003; Salimzadeh & Khalili, 2015). This model, however, does require domain separation, interaction, and regularization as inherently required by its DPDP part.

In this paper, we first establish a fluid-solid fully coupled model of a poroelastic DFN-matrix system. The DFN we consider is of an arbitrary distribution. To circumvent the complications associated with the aforementioned DPDP-based model, we instead retain the classic framework of Biot poroelasticity and formulate the coupled problem over an integrated fracture-matrix domain. This involves not only the redefinition of relevant quantities but also the addition of a separate set of fluid and solid constitutive laws for the fractures. In the fluid problem, we consider highly conductive fractures that behave as hydraulic weak discontinuities. The mass exchange between fractures and the matrix is accounted for by admitting the jump in the normal flow velocity (fluid flux) across fractures. Local mass conservation is also enforced across fractures that are fully immersed within the matrix. We also include nonlinearity arising from pressure-dependent permeability of fractures in the model. In the solid problem, we focus on the state prior to mechanical failure only. Nonetheless, each fracture is considered as a finite-thickness shear deformation zone, which can lead to high degree of heterogeneity in the strain and stress. We then provide a complete hybrid-dimensional computational approach for solving the proposed nonlinear model in a fully coupled, fully implicit manner. Along the way, we demonstrate how the effect of fractures is systematically reflected in the final fully discrete form of the coupled equations.

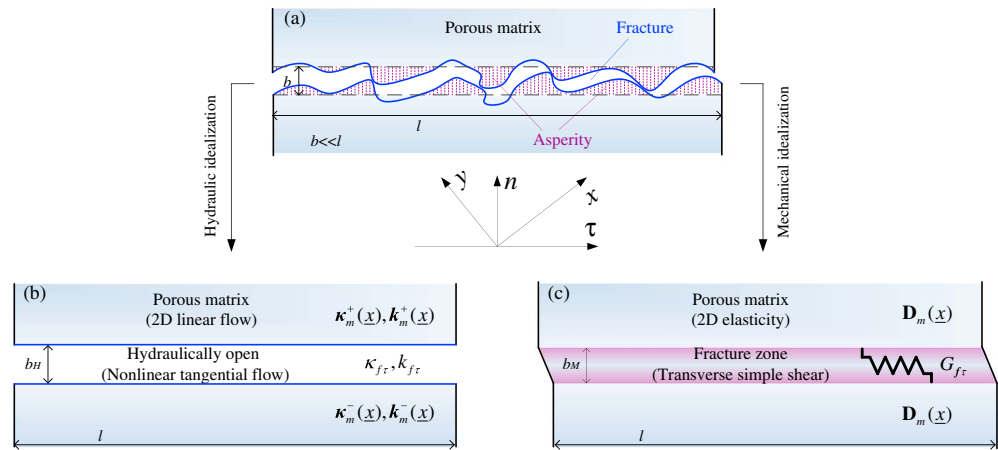


**Figure 1.** A discrete fracture-matrix system. (a) The physical domain consisting of a porous matrix and a fracture. (b) The fracture is hydraulically open with an aperture  $b_H$ . (c) Prior to failure, the fracture acts as a deformation zone sandwiched between the matrix and has a thickness  $b_M$ .

The organization of the paper is as follows. In section 2, we introduce some important assumptions pertaining to fractures, define two model domains, and examine the fluid mass conservation law, the solid force balance law, and the two sets of fluid and solid constitutive laws for both the matrix and fractures. Boundary and interface conditions are also presented to close the system. Section 3 presents the weak formulation of the coupled problem. We show that hybrid-dimensionality can be achieved based on a transversal uniformity assumption across fractures. In section 4, we discretize the fully coupled equations in space and time. In particular, we introduce a hybrid-dimensional, equal-order, two-field mixed finite element method for space discretization. The linearization scheme is provided in section 5, and a numerical example demonstrating the application of the computational model is provided in section 6. Finally, a summary and some conclusions are presented in section 7.

## 2. Mathematical Model

### 2.1. Representation of a Discrete Fracture-Matrix System

To facilitate the model setup, we first introduce the hydraulic and mechanical representations of a fractured porous medium. Consider a 2-D physical domain composed of a fracture embedded within a porous matrix in  $\underline{x}$  (see Figure 1a). We define a fracture as a pair of irregularly shaped surfaces spanning length  $l$  along  $\tau$ . For the fluid problem (Figure 1b), we assume that due to the complex surface roughness, there is always open space for fluid flow; thus, the fracture is hydraulically open and can be simplified into a pair of parallel plates with an effective hydraulic aperture  $b_H$  along  $n$ . For the solid problem (Figure 1c), we assume that the two fracture surfaces are mechanically in contact and interlocked through asperities and morphological irregularities, such that even prior to failure, the fracture effectively acts as a deformation zone with separate compliance and can be simplified into a mechanical layer of thickness  $b_M$ . Consideration of such a “fracture zone” has been shown to be important in a general model (Hu et al., 2017). In terms of application, for example, it can play a protective role and reduce the potential for induced seismicity (Rohmer et al., 2015). Within the matrix, 2-D linear fluid flow and 2-D linear elasticity are assumed. Within the fracture, because of its exceedingly high tangential-to-transversal aspect ratio ( $b_H, b_M \ll l$ ), we consider only tangential fluid flow and transverse simple shear (defined in section 2.4), which are assumed uniform across  $b_H$  and  $b_M$ , respectively. The  $b_M$  is assumed independent from  $b_H$ . In addition, the fluid conduction within the fracture is considered as nonlinear.

### 2.2. Computational Domain and Asymptotic Domain

We now construct a DFN-matrix system in  $\underline{x}$  by defining a 2-D computational domain  $\Omega \subset \mathbb{R}^2$  bounded by  $\partial\Omega$  with an outward normal  $\underline{n}$  (see Figure 2a). The  $\Omega$  consists of a porous matrix domain  $\Omega_m$  and a DFN domain  $\Omega_f$ .  $\Omega_m, \Omega_f \subset \mathbb{R}^2$ , and  $\Omega_m \cup \Omega_f = \Omega$ . The  $\Omega_m$  and  $\Omega_f$  are bounded by their respective boundaries  $\partial\Omega_m$  and  $\partial\Omega_f$ . The  $\Omega_f$  is embedded within  $\Omega_m$  but is allowed to intersect with  $\partial\Omega$ . Consider also that the DFN contains an arbitrary

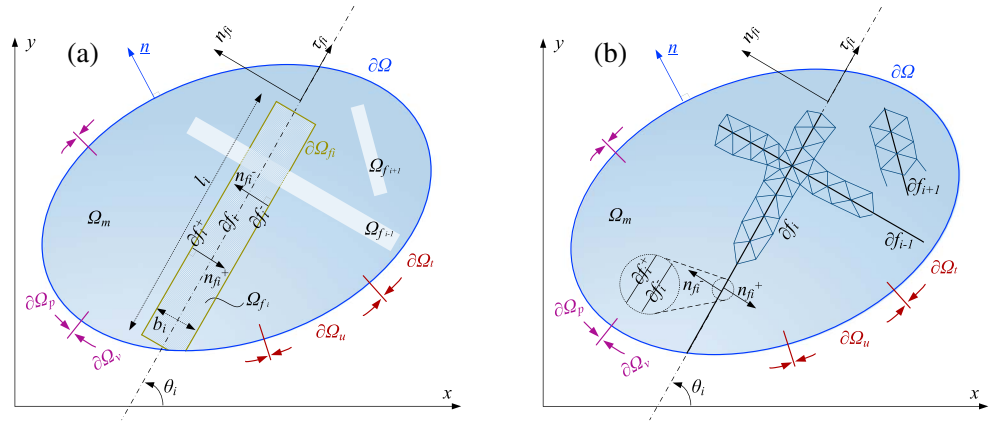


**Figure 2.** A DFN-matrix system. (a) The computational domain  $\Omega$  in which the fracture aperture and thickness are accounted for (b) the asymptotic domain  $\Omega^{asy}$  in which the fracture is vanishingly thin. The coupled conservation laws are formulated and discretized in  $\Omega^{asy}$ , but the fluid and solid constitutive laws are implemented in  $\Omega$  in order to account for fracture aperture and thickness.

set of fully or partially interconnected fractures such that  $\Omega_f = \cup_{i=1}^{n_f} \Omega_{f_i}$ , where  $n_f$  is the number of discrete fractures,  $i$  is the fracture index, and  $\Omega_{f_i}$  denotes the domain occupied by the  $i$ th fracture bounded by  $\partial\Omega_{f_i}$ . The  $\Omega_{f_i}$  is quadrilateral for computational purposes, with a length  $l_i$  along  $\tau_{f_i}$  and an aperture/thickness  $b_i$  along  $n_{f_i}$ ,  $b_i \ll l_i$ . Here  $b$  refers to both  $b_H$  and  $b_M$ . Along  $\tau_{f_i}$ , the midline is denoted as  $\partial f_i$  and the two parallel edges are denoted as  $\partial f_i^+$  and  $\partial f_i^-$ , with outward unit normal vectors denoted as  $\underline{n}_{f_i}^+$  and  $\underline{n}_{f_i}^-$ . Counterclockwise, the angle between the  $x$  axis and  $\partial f_i$  is denoted as  $\theta_i$ . We define  $\underline{n}_{f_i}^- = -\underline{n}_{f_i}^+ = (-\sin\theta_i, \cos\theta_i)^T$ .

Given that  $b_i \ll l_i$ , we also define an asymptotic domain  $\Omega^{asy} \subset \mathbb{R}^2$  (see Figure 2b), in which we let  $b_i$  be vanishingly thin, such that  $\Omega_{f_i}^{asy} \rightarrow \partial f_i$ , and the DFN reduces to a lower dimensional manifold  $\partial f = \cup_{i=1}^{n_f} \partial f_i$  embedded within  $\Omega_m$ . In  $\Omega^{asy}$ ,  $\Omega_m = \Omega^{asy}$ ,  $\partial\Omega$  is the external boundary, and  $\partial f_i^+$ ,  $\partial f_i^-$ , ( $i = 1 \sim n_f$ ) are considered as the internal discontinuities.

We have assumed (section 2.1) that the tangential fluid flux and the simple shear strain are uniform within each fracture. In order to establish a relationship between  $\Omega$  and  $\Omega^{asy}$  and facilitate a hybrid-dimensional approach, we also make the same assumption about their virtual counterparts, such that  $\forall i \in [1, n_f]$ :

$$\begin{aligned} \iint_{\Omega_{f_i}} f(\nabla TF, \nabla PU) d\Omega &= b_{Hi} \int_{\partial f_i} f(\nabla_\tau TF, \nabla_\tau PU) d\Gamma \\ \iint_{\Omega_{f_i}} f(\nabla TE, \nabla PE) d\Omega &= b_{Mi} \int_{\partial f_i} f(\nabla_n TE_{\tau_{f_i}}, \nabla_n PE_{\tau_{f_i}}) d\Gamma \end{aligned} \tag{1}$$

where  $TF, PU$  and  $TE, PE$  are the test functions and the primary unknowns for the fluid problem and the solid problem, respectively. For the fluid problem, we refer to Karimi-Fard & Firoozabadi (2003) for a similar assumption. In this manner,  $b_i$  need not be explicitly resolved during meshing, rather, can be implicitly accounted for during computation. Also, we neglect herein the area occupied by fracture intersections and adopt the following approximation of the integration over  $\Omega_f$  during computation:

$$\int_{\Omega_f} (\cdot) d\Omega = \sum_i \int_{\Omega_{f_i}} (\cdot) d\Omega \tag{2}$$

The external boundary  $\partial\Omega$  is partitioned into  $\partial\Omega_p$  and  $\partial\Omega_v$  for the fluid problem and  $\partial\Omega_u$  and  $\partial\Omega_t$  for the solid problem. Here  $\partial\Omega_p$  and  $\partial\Omega_u$  are Dirichlet boundaries, and  $\partial\Omega_v$  and  $\partial\Omega_t$  are Neumann boundaries. As usual,  $\partial\Omega_p \cap \partial\Omega_v = \emptyset$ ,  $\partial\Omega_p \cup \partial\Omega_v = \partial\Omega$ ;  $\partial\Omega_u \cap \partial\Omega_t = \emptyset$ ,  $\partial\Omega_u \cup \partial\Omega_t = \partial\Omega$ ; and  $\partial\Omega_p \neq \emptyset$ ,  $\partial\Omega_u \neq \emptyset$ . Here  $\emptyset$  denotes a null-space. All domains depend on a time interval of interest  $(0, T)$ .

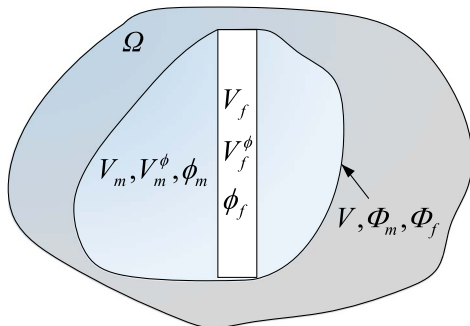


**Figure 3.** Schematic illustration on intrinsic porosities of the matrix and the fracture, which are used to define partial porosities over an amalgamated volume.

### 2.3. The Transient Fluid Problem With Solid-to-Fluid Coupling

Consider an arbitrary, heterogeneous, and anisotropic control volume  $V(\underline{x}, t)$  on  $\Omega \times (0, T)$ ; see Figure 3. We denote its mutually exclusive matrix and fracture volumetric portions as  $V_m(\underline{x}, t)$  and  $V_f(\underline{x}, t)$  and further denote the pore space within  $V_m(\underline{x}, t)$  and  $V_f(\underline{x}, t)$  as  $V_m^\phi(\underline{x}, t)$  and  $V_f^\phi(\underline{x}, t)$ , respectively.

We define and distinguish the following two sets of porosities

$$\begin{aligned}\phi_m(\underline{x}, t) &:= \frac{V_m^\phi(\underline{x}, t)}{V_m(\underline{x}, t)} \\ \phi_f(\underline{x}, t) &:= \frac{V_f^\phi(\underline{x}, t)}{V_f(\underline{x}, t)}\end{aligned}\quad (3)$$

$$\begin{aligned}\Phi_m(\underline{x}, t) &:= \frac{V_m^\phi(\underline{x}, t)}{V(\underline{x}, t)} = \frac{V_m(\underline{x}, t)}{V_m(\underline{x}, t) + V_f(\underline{x}, t)} \quad \phi_m(\underline{x}, t) = \Lambda(\underline{x}, t)\phi_m(\underline{x}, t) \\ \Phi_f(\underline{x}, t) &:= \frac{V_f^\phi(\underline{x}, t)}{V(\underline{x}, t)} = \frac{V_f(\underline{x}, t)}{V_m(\underline{x}, t) + V_f(\underline{x}, t)} \quad \phi_f(\underline{x}, t) = (1 - \Lambda(\underline{x}, t))\phi_f(\underline{x}, t) \\ \Phi(\underline{x}, t) &:= \frac{V_m^\phi(\underline{x}, t) + V_f^\phi(\underline{x}, t)}{V(\underline{x}, t)} = \Phi_m(\underline{x}, t) + \Phi_f(\underline{x}, t)\end{aligned}\quad (4)$$

where, the first set of porosities,  $\phi_m(\underline{x}, t)$  and  $\phi_f(\underline{x}, t)$ , are defined within the matrix domain and the fracture domain, respectively, whereas the second set of porosities,  $\Phi_m(\underline{x}, t)$  and  $\Phi_f(\underline{x}, t)$ , are defined over an amalgamated fracture-matrix domain. The  $\Phi(\underline{x})$  is the total porosity of  $V(\underline{x})$ . Herein, we refer to  $\phi$  and  $\Phi$  as the intrinsic porosity and the partial porosity. The  $\Lambda(\underline{x})$  is a locally defined parameter which is dependent on the supplied matrix-DFN geometric configuration.

Assuming that the medium is fully saturated and taking advantage of the definition of  $\Phi(\underline{x})$ , we can write down the conservation of mass for a transient single-phase fluid over  $\Omega \rightarrow \Omega^{\text{asy}}$ , by recalling the classic statement without the need for separation between  $\Omega_m$  and  $\Omega_f$ :

$$\partial_t(\rho(\underline{x}, t)(\Phi_m(\underline{x}, t) + \Phi_f(\underline{x}, t) - \alpha \nabla \cdot \underline{u}(\underline{x}, t))) + \nabla \cdot (\rho(\underline{x}, t)\underline{v}(\underline{x}, t)) = S(\underline{x}, t) \quad \text{in } \Omega \rightarrow \Omega^{\text{asy}} \times (0, T) \quad (5)$$

where  $\rho(\underline{x}, t)$  is the fluid density;  $\underline{v}(\underline{x}, t)$  is the flow velocity, which is related to the fluid pressure via fluid constitutive laws;  $S(\underline{x}, t)$  is the external fluid source/sink;  $\alpha$  is the Biot-Willis coefficient; and  $\underline{u}(\underline{x}, t)$  is the change in the displacement of the solid skeleton due to the change in the fluid pressure (defined by equation (6)). We note that, here, the fluid problem is formulated over an integrated matrix-fracture domain; the mass exchange between  $\Omega_m$  and  $\Omega_f$  as will be shown later, is included in the divergence term. This differs from the classical dual-porosity double-permeability (DPDP) model (see Appendix A.1), in which two mass conservation laws are separately formulated over  $\Omega_m$  and  $\Omega_f$  and the two interact through a common mass exchange term; additionally, in the DPDP model, the porosity is equivalent to the intrinsic porosity described in equation (3), and the shape factor is the counterpart of  $\Lambda(\underline{x})$ , which is geometry-dependent. However, it is worth noting that here no upscaling is required for calculating  $\Lambda(\underline{x})$  (see Appendix A.3).

In equation (5), the solid-to-fluid coupling effect is given by the coupling term  $-\alpha \nabla \cdot \underline{u}(\underline{x}, t)$ , which quantifies the change in the porosity (see Appendix A.2 for details). Here  $\nabla \cdot \underline{u}(\underline{x}, t)$  is the volumetric strain, which follows a compressive strain positive notation in order to be consistent with the solid problem (section 2.4). Positive volumetric strain correlates with a reduction (negative change) in the porosity, therefore notice the negative sign in front of the coupling term. This is slightly different from a commonly used formulation that follows an extensional strain positive notation, in which case the coupling term becomes positive.

The goal is to solve for the change in the fluid pressure,  $p(\underline{x}, t)$ , defined as

$$p(\underline{x}, t) := p_1(\underline{x}, t) - p_0(\underline{x}) \quad (6)$$

where  $p_0(\underline{x})$  is the initial fluid pressure and  $p_1(\underline{x}, t)$  is the new fluid pressure after perturbation. For brevity, we herein refer to  $p(\underline{x}, t)$  simply as the fluid pressure.

Denote the compressibility of the fluid, the matrix pore, and the fracture as  $C_p$ ,  $C_m$ , and  $C_f$ . They are defined as the following:

$$\begin{aligned} C_p &::= \frac{1}{\rho_0} \frac{d\rho}{dp} \\ C_m &::= \frac{1}{\Phi_{m0}} \frac{d\Phi_m}{dp} \\ C_f &::= \frac{1}{\Phi_{f0}} \frac{d\Phi_f}{dp} \end{aligned} \quad (7)$$

where  $\rho_0$  is the initial fluid density and  $\Phi_{m0}(\underline{x})$  and  $\Phi_{f0}(\underline{x})$  are the initial partial porosities of the matrix and the fracture, respectively.

Consulting equation (4), and letting  $\Lambda(\underline{x}, 0) = \Lambda_0(\underline{x})$ ,  $\phi_{m0}(\underline{x}, 0) = \phi_{m0}(\underline{x})$ , and  $\phi_{f0}(\underline{x}, 0) = \phi_{f0}(\underline{x})$ , one finds

$$\begin{aligned} \Phi_{m0}(\underline{x}) &= \Lambda_0(\underline{x}) \phi_{m0}(\underline{x}) \\ \Phi_{f0}(\underline{x}) &= (1 - \Lambda_0(\underline{x})) \phi_{f0}(\underline{x}) \end{aligned} \quad (8)$$

Here  $\Lambda_0(\underline{x})$  can be calculated based on the initial matrix-fracture configuration (see Appendix A.3 and equation (A4)). Furthermore, for the fluid problem, it is common to consider a fracture as a full empty space (e.g., Garipov et al., 2016; Mustapha, 2014), which is consistent with the fracture hydraulic representation in section 2.1. In  $\Omega$ , this reads

$$\phi_{f0}(\underline{x}) \equiv \begin{cases} 1, & \forall \underline{x} \in \Omega_f \\ 0, & \forall \underline{x} \in \Omega \setminus \Omega_f = \Omega_m \end{cases} \quad (9)$$

The total time derivatives of the density, the partial porosity, and the solid displacement take the following canonical form:

$$\begin{aligned} \dot{\rho}(\underline{x}, t) &= \partial_t \rho(\underline{x}, t) + \nabla \rho(\underline{x}, t) \cdot \underline{v}_p \\ \dot{\Phi}_r(\underline{x}, t) &= \partial_t \Phi_r(\underline{x}, t) + \nabla \Phi_r(\underline{x}, t) \cdot \underline{v}_s, \quad r = m, f \\ \dot{\underline{u}}(\underline{x}, t) &= \partial_t \underline{u}(\underline{x}, t) + \nabla \underline{u}(\underline{x}, t) \cdot \underline{v}_s \end{aligned} \quad (10)$$

where  $\underline{v}_p$  and  $\underline{v}_s$  are the velocity of the fluid and the solid skeleton, respectively.

Next, we make the following two approximations:

$$\nabla \rho(\underline{x}, t) \approx 0 \quad (11)$$

$$\underline{v}_s(\underline{x}, t) \approx 0 \quad (12)$$

Equation (11) is a common underlying assumption made in standard reservoir simulation formulations (e.g., Aziz & Settari, 1979) and many coupled formulations (e.g., Castelletto et al., 2015a; Jha & Juanes, 2007). It allows approximation of the divergence of the fluid flux using the initial fluid density. Equation (12) arises from an assumption of quasi-static deformation (section 2.4). Equations (11) and (12) therefore allow approximation of the partial time derivatives of relevant variables using their respective total time derivatives shown in equation (10).

In addition, by definition, the initial change in the volumetric strain due to the fluid pressure is 0:

$$\nabla \cdot \underline{u}(\underline{x}, 0) = 0 \quad (13)$$

Expanding the left-hand side (LHS) of equation (5), substituting in equations (7)–(13), dividing both sides by  $\rho_0$  and writing  $S(\underline{x}, t)/\rho_0$  as  $s(\underline{x}, t)$  yields

$$\begin{aligned} &(\Lambda_0(\underline{x}) \phi_{m0}(\underline{x}) (C_m + C_p) + (1 - \Lambda_0(\underline{x})) \phi_{f0}(\underline{x}) (C_f + C_p)) \dot{p}(\underline{x}, t) - \alpha \nabla \cdot \dot{\underline{u}}(\underline{x}, t) + \nabla \cdot \underline{v}(\underline{x}, t) \\ &= s(\underline{x}, t) \quad \text{in } \Omega \rightarrow \Omega^{\text{asy}} \times (0, T) \end{aligned} \quad (14)$$

Next, we distinguish two types of fractures: sealing fractures and conductive fractures. Following Martin et al. (2005), in  $\Omega^{\text{asy}}$ , the former leads to pressure discontinuity (hydraulic strong discontinuity), whereas the latter

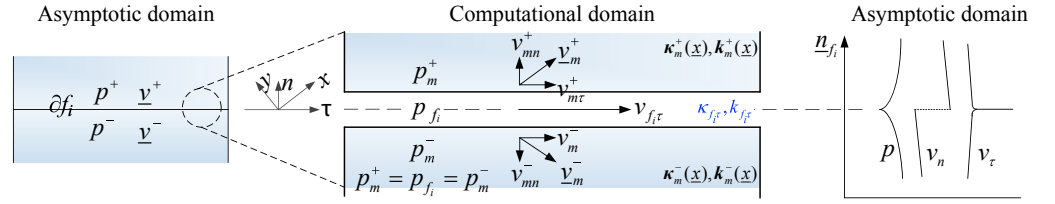


**Figure 4.** Graphic illustration on continuous distribution of the fluid pressure and discontinuous distribution of the flow velocity across a highly conductive fracture. The asymptotic domain is shown on the left and the computational domain in the middle. On the right are profiles of the fluid pressure and the normal and tangential components of the flow velocity in the asymptotic domain. The pressure continuity is naturally enforced via a hybrid-dimensional approach. Uniform tangential flow velocity within the fracture is assumed.

permits flux/velocity discontinuity (hydraulic weak discontinuity) across  $\partial f$ . A sealing fracture typically occurs in the form of a hydraulically inactive fault where the impermeable fault gouge prohibits transversal flow; this type of fracture is not the focus of this study. Here we focus on conductive fractures only. Specifically, we assume that the tangential permeability of  $\Omega_f$  is much higher than any component of the permeability tensor of  $\Omega_m$ . In such cases, it is safe to assume pressure continuity across  $\partial f$  in  $\Omega^{asy}$ . Note that the pressure is not necessarily differentiable across  $\partial f$ . In other words, it is at least  $C^0$  continuous (Luege et al., 2015; Prévost & Sukumar, 2016). Nonetheless, a jump in the fluid normal velocity  $v_n$  (pressure normal gradient) and a spike in the fluid tangential velocity  $v_\tau$  (pressure tangential gradient) across a fracture, are allowed (Meschke & Leonhart, 2015) (see Figure 4). In  $\Omega^{asy}$ , the above statement is summarized as

$$[[p(\underline{x}, t)]] = 0, \quad [[\underline{v}(\underline{x}, t)]] \cdot \underline{n}_i \neq \underline{0}, \quad \forall \underline{x} \in \partial f_i, i = 1 \sim n_f \quad (15)$$

We now write down the two fluid constitutive laws. In  $\Omega_m$ ,  $\underline{v}(\underline{x}, t)$  is given by the 2-D Darcy's law:

$$\underline{v}_m(\underline{x}, t) = -\kappa_m(\underline{x}) \cdot \nabla p_m(\underline{x}, t) = -\eta^{-1} \mathbf{k}_m(\underline{x}) \cdot \nabla p_m(\underline{x}, t) \quad \forall \underline{x} \in \Omega_m \quad (16)$$

where  $p_m(\underline{x}, t)$  is the fluid pressure,  $\eta$  is the fluid viscosity, and  $\kappa_m(\underline{x})$  and  $\mathbf{k}_m(\underline{x})$  are the heterogeneous and fully anisotropic hydraulic conductivity and permeability tensors. Without changing the generality of the method itself, here we consider a simply anisotropic permeability tensor:

$$\mathbf{k}_m(\underline{x}) = \begin{bmatrix} k_{mx}(\underline{x}) & 0 \\ 0 & k_{my}(\underline{x}) \end{bmatrix} \quad (17)$$

In  $\Omega_f$ , it is appropriate to consider the Stokes flow, leading to the so-called Brinkman problem (e.g., Dereims et al., 2015). Here, however, we neglect the free flow effect and consider only transversally uniform 1-D flow along the fracture tangential direction (see, e.g., Martin et al., 2005), as described by the 1-D Darcy's law in a local reference frame:

$$\underline{v}_{f_i\tau}(\underline{x}, t) = \underline{v}_{f_i}(\underline{x}, t) \cdot \underline{\tau}_i = -\kappa_{f_i\tau} \nabla_\tau p_{f_i}(\underline{\xi}, t) = -\eta^{-1} k_{f_i\tau} \nabla_\tau p_{f_i}(\underline{\xi}, t) \quad \forall \underline{x} \in \Omega_{f_i}, i = 1 \sim n_f \quad (18)$$

where  $p_{f_i}(\underline{x}, t) = p_{f_i}(\underline{\xi}, t)$  is the fluid pressure within the  $i$ th fracture,  $p_{f_i}(\underline{x}, t) \subset p_m(\underline{x}, t) = p(\underline{x}, t)$  in  $\Omega^{asy}$ , and  $\kappa_{f_i\tau}$  and  $k_{f_i\tau}$  are the fracture tangential conductivity and permeability, respectively. Here  $k_{f_i\tau}$  can be related to the fracture hydraulic aperture  $b_{Hi}$  according to the cubic law (Witherspoon et al., 1980), which reads the following when the surface roughness and tortuosity effects are neglected:

$$k_{f_i\tau} = \frac{1}{12} b_{Hi}^2, \quad i = 1 \sim n_f \quad (19)$$

Following Formaggia et al. (2014), strong pressure variations may occur at intersections of fractures with radically different conductivities. To ensure pressure continuity, here we further assume  $b_{Hi} \sim b_{Hj} \forall i, j \in [1, n_f]$ . This implies that all fractures have similar tangential permeabilities. In the case of an intersection of fractures with highly contrasting conductivities, a more careful treatment can be applied by adding the pressure at the intersection of fracture center lines as an additional degree of freedom (Schwenck et al., 2015).



In this study, we do not focus on the hydraulic fracturing process; that is, in the solid problem, the displacement across a fracture is continuous and no mechanical strong discontinuity is present. This typically is the case when the fluid pressure within a fracture is insufficient to overcome the normal stress acting on it, and therefore, no opening mode failure is present. Nonetheless, in the fluid problem, the hydraulic property of a fracture is strongly pressure-dependent, and therefore, the flow along the fracture, as described by equations (18) and (19), is nonlinear. To account for this nonlinearity, we consider the following relationship:

$$\frac{db_H(p_f)}{b_{H0}} = \frac{d\Phi_f}{\Phi_{f0}} \quad (20)$$

where  $b_{H0}$  is the initial hydraulic aperture and  $db_H$  is the change due to the change in the pressure.

From equation (20) and the third equation in equation (7), the hydraulic aperture thus becomes

$$b_H = b_{H0} + db_H = b_{H0}(1 + C_f p_f) \quad (21)$$

The above linear-type dependency of hydraulic aperture on the fluid pressure within a fracture has been observed in laboratory experiments (e.g., Walsh, 1981). Substitution of equations (18), (19), and (21) into equation (14) yields a nonlinear equation.

Finally and without losing the generality of our model, we stipulate for now that the external fluid source  $s$  is provided only within  $\Omega_m$ , such that  $s(\underline{x}, t) = 0 \forall \underline{x} \in \Omega_f$ . Changes upon removal of this assumption will be briefly discussed in section 3.1.

#### 2.4. The Quasi-Static Solid Problem With Fluid-to-Solid Coupling

Throughout the solid problem, we use a compressive stress positive notation. Prior to the fluid pressure perturbation, the fluid-filled solid is governed by the quasi-static force balance law, which reads

$$\nabla \cdot (\boldsymbol{\sigma}'_0(\underline{x}) + \alpha p_0(\underline{x})\mathbf{1}) + \underline{f}_b(\underline{x}) = \underline{0} \quad \text{in } \Omega \rightarrow \Omega^{asy} \quad (22)$$

where  $\boldsymbol{\sigma}'_0(\underline{x})$  is the initial effective stress tensor,  $\mathbf{1}$  is the unit identity tensor (Kronecker delta),  $\alpha$  is the Biot-Willis coefficient (see also equation (5)),  $\boldsymbol{\sigma}'_0(\underline{x}) + \alpha p_0(\underline{x})\mathbf{1}$  is the initial Cauchy total stress tensor where the positive sign arises from the sign convention, and  $\underline{f}_b(\underline{x})$  is the body force.

After the fluid pressure perturbation and prior to the occurrence of any dynamic failure, the fluid-filled solid needs to satisfy the following in order to regain quasi-static equilibrium:

$$\nabla \cdot (\boldsymbol{\sigma}'(\underline{x}, t) + \alpha p(\underline{x}, t)\mathbf{1} + \boldsymbol{\sigma}'_0(\underline{x}) + \alpha p_0(\underline{x})\mathbf{1}) + \underline{f}_b(\underline{x}) = \underline{0} \quad \text{in } \Omega \rightarrow \Omega^{asy} \times (0, T) \quad (23)$$

where  $\boldsymbol{\sigma}'(\underline{x}, t)$  is the change in the effective stress tensor due to the change in the fluid pressure,  $p(\underline{x}, t)$ , which is supplied from the fluid problem described in section 2.3. From equations (22) and (23), one finds that  $\boldsymbol{\sigma}'(\underline{x}, t)$  can be solved from

$$\nabla \cdot (\boldsymbol{\sigma}'(\underline{x}, t) + \alpha p(\underline{x}, t)\mathbf{1}) = \nabla \cdot \boldsymbol{\sigma}'(\underline{x}, t) + \underline{f}_p(\underline{x}, t) = \underline{0} \quad \text{in } \Omega \rightarrow \Omega^{asy} \times (0, T) \quad (24)$$

Here  $\underline{f}_p(\underline{x}, t)$  is an equivalent body force vector due to the gradient of the fluid pressure:

$$\underline{f}_p(\underline{x}, t) = \alpha \nabla p(\underline{x}, t) \quad (25)$$

Because the (negative) pressure gradient is directly indicative of the flow velocity in the Darcy flow regime, as is shown by equations (16) and (18), the equivalent body force can thus be discontinuous across a fracture; furthermore,  $\boldsymbol{\sigma}'(\underline{x}, t)$  can be regarded as a flow-driven effective stress tensor due to a fluid-to-solid coupled poroelastic process, which essentially rests on the principle of effective stress. In the presence of fluid flow (fluid in motion),  $\boldsymbol{\sigma}'(\underline{x}, t)$  must be solved from equations (24) and (25), and one should expect that, in general,  $\boldsymbol{\sigma}'(\underline{x}, t) \neq -\alpha p(\underline{x}, t)\mathbf{1}$ . The equal sign can only be drawn when the fluid pressure gradient vanishes (an uniform change in the fluid pressure within the medium), in which case the poroelastic process reduces to a decoupled process. Superimposing  $\boldsymbol{\sigma}'(\underline{x}, t)$  onto  $\boldsymbol{\sigma}'_0(\underline{x})$  yields the final effective stress state which can be used for various analysis accounting for the poroelastic effect.

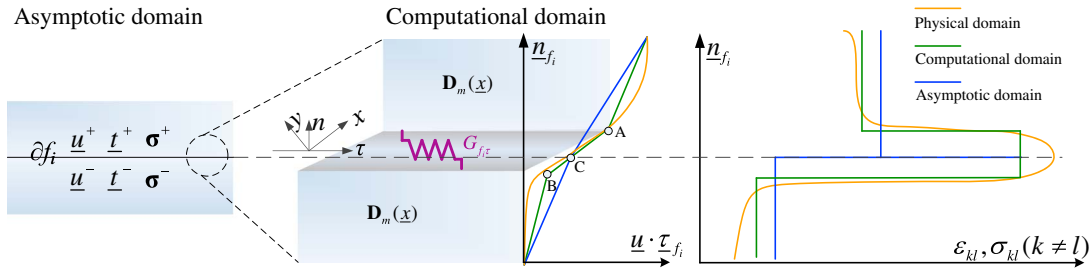


**Figure 5.** Graphic illustration on a fracture as a finite-thickness mechanical zone with transverse simple shear behavior. The strain distribution is shown on the right, the displacement profile is shown in the middle along with the computational domain, and the asymptotic domain is shown on the left. The color of each profile is indicated on the upper right. Continuity in traction and displacement is enforced. A two-step simplification is made to enable the hybrid-dimensional approach, see text.

We choose  $\underline{u}(\underline{x}, t)$  (defined in equation (5)) as the primary unknown for the solid problem. The conceptual model of a fracture is illustrated in Figure 5. First, we restrict our focus on the state prior to occurrence of mechanical failure on the fracture; therefore,  $\underline{u}(\underline{x}, t)$  is at least a  $C^0$  continuous function across  $\partial f$  in  $\Omega^{\text{asy}}$ . Second, as mentioned in section 2.1, we consider a fracture as a finite-thickness fracture zone with transverse simple shear behavior in  $\Omega$ . The presence of this zone allows shear strain concentration within as well as strain heterogeneity across it. Nonetheless, within the mechanically layered solid, the traction is transferred continuously everywhere. We therefore enforce the following continuity conditions for the solid:

$$[[\underline{u}(\underline{x}, t)]] = \underline{0}, \quad [[\underline{t}_f(\underline{x}, t)]] = [[\underline{\sigma}(\underline{x}, t)]] \cdot \underline{n}_f = \underline{0}, \quad \forall \underline{x} \in \partial f_i, i = 1 \sim n_f \quad (26)$$

Figure 5 further illustrates a two-step simplification to facilitate a hybrid-dimensional approach. First, the variation of the shear strain within the fracture zone, if any, is neglected, and instead, uniform shear strain is assumed in  $\Omega$ . This is done by replacing the smooth tangential displacement profile (yellow) with a discretized nonsmooth counterpart (green), resulting in the strain profile to change from smooth but with a sharp variation to step function-like. Second, the thickness of the fracture zone is condensed by collapsing point A, B onto C, and the tangential displacement profile in  $\Omega$  (green) is further approximated with the one in  $\Omega^{\text{asy}}$  (blue), causing the corresponding strain profile to become Heaviside function-like.

We now write down the two solid constitutive laws. For  $\Omega_m$ , we adopt the Hooke's law:

$$\underline{\sigma}'_m(\underline{x}, t) = \mathbf{D}_m : \underline{\varepsilon}_m(\underline{x}, t) = \mathbf{D}_m : \nabla^s \underline{u}_m(\underline{x}, t) \quad \forall \underline{x} \in \Omega_m \quad (27)$$

where  $\underline{\varepsilon}_m(\underline{x}, t)$  and  $\underline{u}_m(\underline{x}, t)$  are the poroelastic strain tensor and the displacement within the matrix,  $\nabla^s$  is the symmetric gradient operator,  $\nabla^s(\cdot) = (\nabla(\cdot) + (\nabla(\cdot))^T)/2$ , and  $\mathbf{D}_m$  is the matrix elastic stiffness tensor. Here we consider a plane strain case, where  $\mathbf{D}_m$  takes the following form:

$$\mathbf{D}_m = \frac{E_m}{(1 + \nu_m)(1 - 2\nu_m)} \begin{bmatrix} 1 - \nu_m & \nu_m & 0 \\ \nu_m & 1 - \nu_m & 0 \\ 0 & 0 & (1 - 2\nu_m)/2 \end{bmatrix} \quad (28)$$

where  $E_m$  and  $\nu_m$  are the Young's modulus and Poisson's ratio of the porous matrix.

Within the fracture zone  $\Omega_f$  we adopt the following linear shear constitutive law described in a local reference frame. Following the standard convention, we denote the poroelastic shear stress as  $\sigma'_{n\tau}$  to show its sense. For the  $i$ th fracture,  $\sigma'_{n\tau}$  reads

$$\sigma'_{n_i\tau_i}(\underline{\xi}, t) = G_{f_i} \gamma_{f_i}(\underline{\xi}, t) \quad \forall \underline{\xi} \in \Omega_{f_i}, i = 1 \sim n_f \quad (29)$$

where  $G_{f_i}$  is the shear modulus of the fracture zone and  $\gamma_{f_i}(\underline{\xi}, t)$  is the poroelastic shear strain, which is assumed to be transversally uniform, hence the name "transverse simple shear." It is defined as

$$\gamma_{f_i}(\underline{\xi}, t) := \frac{\partial u_{f_i\tau}(\underline{\xi}, t)}{\partial n_{f_i}} = \nabla_n u_{f_i\tau}(\underline{\xi}, t) \quad (30)$$

where  $u_{f_i\tau}(\underline{\xi}, t)$  is the tangential displacement related to  $\underline{u}_f(\underline{x}, t)$  via a simple projection (section 4.2) and  $\underline{u}_{f_i}(\underline{x}, t) \subset \underline{u}_m(\underline{x}, t) = \underline{u}(\underline{x}, t)$  in  $\Omega^{\text{asy}}$ .

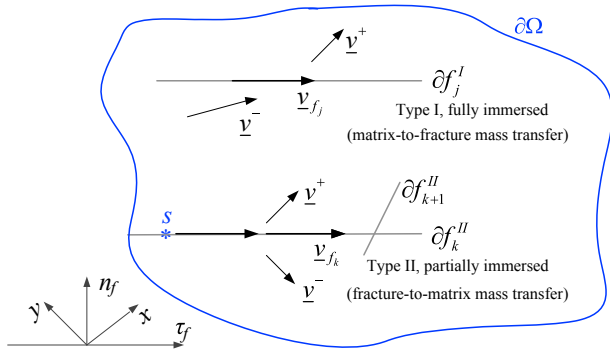


**Figure 6.** Schematic illustration on two types of conductive fractures. A type II fracture  $\partial f^I$  is connected to either the fluid source  $s$  or the boundary  $\partial\Omega$ , and it acts as a preferred flow path, supplying fluid to the surrounding matrix and resulting in a fracture-to-matrix mass transfer. In contrast, a type I fracture  $\partial f^{II}$  is completely immersed within the matrix and can only draw fluid from the surrounding, resulting in a matrix-to-fracture mass transfer.

Consideration of transverse simple shear of a fracture can be found in other studies (e.g., Castelletto et al., 2017).

### 2.5. Boundary, Interface, and Initial Conditions

We wish to model changes in field variables under homogeneous boundary conditions. In  $\Omega^{asy}$ , standard Dirichlet and Neumann boundary conditions are prescribed on  $\partial\Omega$  for both the fluid problem and the solid problem (see, e.g., Meschke & Leonhart, 2015):

$$p(\underline{x}) = p_g \quad \forall \underline{x} \in \partial\Omega_p \quad (31)$$

$$-\underline{n} \cdot \underline{v}(\underline{x}) = v_h \quad \forall \underline{x} \in \partial\Omega_v \quad (32)$$

$$\underline{u}(\underline{x}) = \underline{u}_g \quad \forall \underline{x} \in \partial\Omega_u \quad (33)$$

$$\underline{n} \cdot \underline{\sigma}(\underline{x}) = \underline{t}_i(\underline{x}) \quad \forall \underline{x} \in \partial\Omega_t \quad (34)$$

To close the boundary value problem, the above boundary conditions must be augmented by their counterparts on the internal discontinuity  $\partial f$ . In principal,  $\partial f$  can also be partitioned into Dirichlet and Neumann types. However, usually, Neumann conditions alone are sufficient to account for (1) the mass exchange between  $\Omega_f$  and  $\Omega_m$  through fluid flux in the fluid problem and (2) either a traction-free condition or a continuous traction condition across  $\partial f$  in the solid problem.

In the fluid problem, we assume that no inflow is injected into and no outflow is extracted from any fracture at a known rate; thus, the counterpart of equation (32) can be omitted. On the other hand, certain matrix-fracture interface conditions ought to be met. To examine these conditions, we first divide the fractures in this study (conductive fractures as opposed to sealing fractures) into two groups: fully immersed fractures (type I) and partially immersed fractures (type II), denoted as  $\partial f^I$  and  $\partial f^{II}$ , respectively. Here  $\partial f^I = \cup_{j=1}^{n_f} \partial f_j^I$ ,  $\partial f^{II} = \cup_{k=1}^{n_{fII}} \partial f_k^{II}$ , where  $n_{fI}$  and  $n_{fII}$  are the numbers of the two types of fractures. The  $\partial f^I$  does not intersect the external boundary  $\partial\Omega$  upon which equations (31)–(34) are imposed, nor the area where the source/sink term is specified (see also section 2.3), whereas  $\partial f^{II}$  implies otherwise; see Figure 6.

On  $\partial f^I$ , the tangentially diffusing fluid originates only from the matrix; thus, the following velocity interface condition, which accounts for the matrix-to-fracture mass transfer, is required (see, e.g., Angot et al., 2009; Antonietti et al., 2015; Faille et al., 2016; Martin et al., 2005):

$$-[[\underline{v}(\underline{x}, t)]] \cdot \underline{n}_f = \nabla_\tau \cdot (\underline{v}_f(\underline{x}, t) b_{Hj}), \quad \forall \underline{x} \in \partial f_j^I, j = 1 \sim n_f \quad (35)$$

where  $\nabla_\tau$  is the tangential divergence operator.

Integrating equation (35) over  $\partial f_j^I$ , recognizing the tangentially invariant  $b_{Hj}$ , and applying Gauss theorem on the right-hand side (RHS) lead to the recovery of the local mass balance, which reads

$$-\int_{\partial f_j^I} [[\underline{v}(\underline{x}, t)]] \cdot \underline{n}_f d\Gamma = \int_{\Omega_j} \nabla_\tau \cdot \underline{v}_f(\underline{x}, t) d\Omega = \int_{\partial f_j^I} \underline{v}_f(\underline{x}, t) \cdot \underline{\tau}_f d\Gamma = \int_{\partial f_j^I} v_{f\tau}(\underline{x}, t) d\Gamma \quad (36)$$

Because the permeability on  $\partial f^I$  is orders of magnitude higher than that of the surrounding matrix, fractures act as preferred flow paths. These paths are associated with much shorter characteristic diffusion times, such that the next fracture  $\partial f_{k+1}^{II}$  always draws source fluid from the previous fracture  $\partial f_k^I$  connected to it (see Figure 6) rather than from the immediately surrounding matrix. In such cases, a fracture-to-matrix mass transfer is appropriate. It can be represented by the normal velocity jump,  $[[\underline{v}(\underline{x}, t)]] \cdot \underline{n}$  which is independent from the remaining flow  $\underline{v}_f(\underline{x}, t)$  along the fracture. No interface condition is required.

We note that boundary conditions at fracture-fracture intersections (e.g., Pouya, 2012) and fracture-external boundary intersections (e.g., Antonietti et al., 2015) are not considered. The viscous drag is also neglected, and the so-called Beavers-Joseph interface condition (Beavers & Joseph, 1967) is not included.

For the solid problem, the fractures are in contact. Thus, traction continuity is a required interface condition, as is given in equation (26).

Finally, the initial conditions for the coupled system read

$$p(\underline{x}, 0) = 0 \quad \forall \underline{x} \in \Omega \setminus \partial\Omega_p \quad (37)$$

$$\underline{u}(\underline{x}, 0) = \underline{0} \quad \forall \underline{x} \in \Omega \setminus \partial\Omega_u \quad (38)$$

### 3. Weak Formulation: A Hybrid-Dimensional Approach

The weak formulations of the conservation law (equation (14)) and the balance law (equation (24)) can be obtained following standard procedures (see, e.g., Hughes, 2012), except that here we adopt a hybrid-dimensional representation of the DFN-matrix system and integrate directly over  $\Omega^{\text{asy}}$  rather than  $\Omega$ . Since fractures are considered as internal boundaries of lower dimensions in  $\Omega^{\text{asy}}$ , we invoke the extended divergence theorem to push the volume integral onto  $\partial\Omega$  as well as  $\partial f_i^+$  and  $\partial f_i^-$  ( $i \in [1, n_f]$ ) (Figure 2b). This will allow us to account for weak discontinuities across fractures, if any exist. As mentioned in section 2.2, the fluid and solid constitutive laws for both the matrix domain  $\Omega_m$  and the fracture domain  $\Omega_f$  will be implemented in  $\Omega$  (Figure 2a). Specifically, this means that when the gradients of the primary unknowns appear independently, we can decompose the volume integration over  $\Omega^{\text{asy}} \rightarrow \Omega$  into the summation of two integrations over  $\Omega_m$  and  $\Omega_f$ . Further, the two assumptions stated by equations (1) and (2) will allow a reduction from a volume integration over  $\Omega_f$  into a surface integration along  $\partial f_i$ . The complete weak formulations will consist of a 2-D integration over  $\Omega^{\text{asy}}$  and 1-D integration over  $\partial f_i$ . Meanwhile,  $b_{Hi}$  and  $b_{Mi}$  in equation (1) ensure dimensional consistency. For brevity, we omit writing  $(\underline{x}, t)$  and  $(t)$  following relevant space- and time-dependent variables in this section.

#### 3.1. The Fluid Problem With Solid-to-Fluid Coupling

Let a scalar quantity  $w \in \{w: \Omega \rightarrow \mathbb{R}^2 \mid w \in H^1, w=0 \text{ on } \partial\Omega_p\}$ . Here  $H^1$  is a Sobolev space of degree one. Multiplying equation (14) by  $w$ , integrating over  $\Omega^{\text{asy}}$ , and performing integration by parts on the divergence term on LHS lead to the following:

$$\begin{aligned} & \underbrace{\iint_{\Omega^{\text{asy}}} w \Lambda_0 \phi_{m0} (C_m + C_p) \dot{p} d\Omega}_{\Omega \leftarrow \Omega^{\text{asy}} = \Omega_m} + \underbrace{\iint_{\Omega^{\text{asy}}} w (1 - \Lambda_0) \phi_{f0} (C_f + C_p) \dot{p} d\Omega}_{\Omega_m \cup \Omega_f = \Omega \leftarrow \Omega^{\text{asy}}} - \underbrace{\iint_{\Omega^{\text{asy}}} w \alpha (\nabla \cdot \underline{u}) d\Omega}_{\Omega \leftarrow \Omega^{\text{asy}} = \Omega_m} \\ & + \underbrace{\iint_{\Omega^{\text{asy}}} \nabla \cdot (w \underline{v}) d\Omega}_{\Omega \leftarrow \Omega^{\text{asy}} = \Omega_m} - \underbrace{\iint_{\Omega^{\text{asy}}} \nabla w \cdot \underline{v} d\Omega}_{\Omega_m \cup \Omega_f = \Omega \leftarrow \Omega^{\text{asy}}} = \underbrace{\iint_{\Omega^{\text{asy}}} w s d\Omega}_{\Omega \leftarrow \Omega^{\text{asy}} = \Omega_m} \end{aligned} \quad (39)$$

The second term on the LHS is fracture-related and is expanded in  $\Omega$ . Considering equation (9) and subsequently equation (2), one finds

$$\begin{aligned} & \iint_{\Omega^{\text{asy}} \rightarrow \Omega} w (1 - \Lambda_0) \phi_{f0} C_f \dot{p} d\Omega \\ & = \iint_{\Omega_m} w (1 - \Lambda_0) \phi_{f0} C_f \dot{p} d\Omega + \iint_{\Omega_f} w (1 - \Lambda_0) \phi_{f0} C_f \dot{p} d\Omega \\ & = \sum_{i \in n_f} \int_{\partial f_i} w (1 - \Lambda_0) \phi_{f0} C_f \dot{p} b_i d\Gamma \end{aligned} \quad (40)$$

Here one underlying requirement is that  $\Lambda_0(\underline{x})$  is transversely uniform. As will be shown in section 4, this requirement can be effectively met as  $\Lambda_0(\underline{x})$  is constant element-wise.

The fourth term on the LHS of equation (39) can be calculated by invoking the extended divergence theorem to admit the normal discontinuity in fluid flux across each fracture (see, e.g., Armero & Callari, 1999; Pouya, 2015; Prévost & Sukumar, 2016). Here we further distinguish between fully immersed and partially immersed fractures:

$$\iint_{\Omega^{\text{asy}}} \nabla \cdot (w \underline{v}) d\Omega = \int_{\partial\Omega} w \underline{v} \cdot \underline{n} d\Gamma - \sum_{j \in n_f} \int_{\partial f_j^+} w [\underline{v}] \cdot \underline{n}_j d\Gamma - \sum_{k \in n_m} \int_{\partial f_k^+} w [\underline{v}] \cdot \underline{n}_k d\Gamma \quad (41)$$

where the first normal velocity jump, which represents the matrix-to-fracture mass transfer on fully immersed fractures, is linked to the interface condition presented in equation (36). The second normal velocity jump

represents the fracture-to-matrix mass transfer on partially immersed fractures and can be rewritten as the following (Noetinger, 2015; Noetinger & Jarrige, 2012):

$$\left[ \underline{v} \right] \cdot \underline{n}_{f_k} = -[\kappa_m \cdot \nabla p_m] \cdot \underline{n}_{f_k} \Big|_{\partial f_k^m} = -[\kappa_m \cdot \nabla p] \cdot \underline{n}_{f_k} \Big|_{\partial f_k^m} \quad (42)$$

In the fifth term on the LHS of equation (39),  $\underline{v}$ , which calls for the two sets of fluid constitutive laws, appears independently within the integral. We expand it in  $\Omega$ , honor equation (2) and then equation (1), and substitute in equations (16) and (18):

$$\begin{aligned} \iint_{\Omega^{\text{asy}} \rightarrow \Omega} \nabla W \cdot \underline{v} d\Omega &= \iint_{\Omega_m} \nabla W \cdot \underline{v}_m d\Omega + \iint_{\Omega_f} \nabla W \cdot \underline{v}_f d\Omega \\ &= -\iint_{\Omega_m} \nabla W \cdot \kappa_m \cdot \nabla p d\Omega - \sum_{i \in n_f} b_{Hi} \int_{\partial f_i} \nabla_\tau W \cdot \kappa_{f_i \tau} \nabla_\tau p d\Gamma \end{aligned} \quad (43)$$

Finally, since we have assumed that the external fluid source is provided only within the matrix domain, the integration on the RHS of equation (39) can be completed over  $\Omega^{\text{asy}}$  without expansion in  $\Omega$ . Relaxation of this assumption will then require a similar decomposition process described above. In this case, one would then need to specify a separate source/sink term for the fractures.

Substituting equations (40)–(43) into equation (39), noticing the Neumann boundary condition equation (32) and the interface condition equation (36), and noticing  $\Omega^{\text{asy}} = \Omega_m$ , we obtain the final weak formulation of the fluid problem:

$$\begin{aligned} &\iint_{\Omega_m} w \Lambda_0 \phi_{m0} (C_m + C_\rho) \dot{p} d\Omega + \sum_{i \in n_f} b_{Hi} \int_{\partial f_i} w (1 - \Lambda_0) \phi_{f,0} (C_{f_i} + C_\rho) \dot{p} d\Gamma \\ &- \iint_{\Omega_m} w \alpha (\nabla \cdot \underline{u}) d\Omega \\ &+ \iint_{\Omega_m} \nabla W \cdot \kappa_m \cdot \nabla p d\Omega + \sum_{i \in n_f} b_{Hi} \int_{\partial f_i} \nabla_\tau W \cdot \kappa_{f_i \tau} \nabla_\tau p d\Gamma \\ &- \sum_{j \in n_f} \int_{\partial f_j} w \kappa_{f_j \tau} \nabla_\tau p d\Gamma + \sum_{k \in n_f} \int_{\partial f_k^m} w [[\kappa_m \cdot \nabla p]] \cdot \underline{n}_{f_k} d\Gamma \\ &= \int_{\partial \Omega_v} w v_h d\Gamma + \iint_{\Omega_m} w s d\Omega \end{aligned} \quad (44)$$

### 3.2. The Solid Problem With Fluid-to-Solid Coupling

Let a vector quantity  $\underline{\eta} \in \left\{ \underline{\eta} : \Omega \rightarrow \mathbb{R}^2 \mid \underline{\eta} \in \mathbf{H}^1, \underline{\eta} = \underline{0} \text{ on } \partial \Omega_u \right\}$ . Again,  $\mathbf{H}^1$  is a Sobolev space of degree one. Similarly, multiplying equation (24) with  $\underline{\eta}$ , integrating over  $\Omega^{\text{asy}}$ , and performing integration by part, on one side, decomposing the total stress into the sum of the effective stress and the pore pressure, we have (here we use symbolic notation and indicial notation interchangeably)

$$\underbrace{\iint_{\Omega^{\text{asy}}} \eta_{l,k} \sigma'_{kl} d\Omega}_{\Omega_m \cup \Omega_f = \Omega \leftarrow \Omega^{\text{asy}}} + \underbrace{\iint_{\Omega^{\text{asy}}} \eta_{l,k} \alpha p \delta_{kl} d\Omega}_{\Omega \leftarrow \Omega^{\text{asy}} = \Omega_m} = \underbrace{\iint_{\Omega^{\text{asy}}} (\eta_l \sigma_{kl})_{,k} d\Omega}_{\Omega \leftarrow \Omega^{\text{asy}} = \Omega_m} \quad (45)$$

For the first term on the LHS, because  $\sigma'_{kl}$  calls for the two sets of solid constitutive laws, we decompose the integration into the summation of two integrations over  $\Omega_m$  and  $\Omega_f$ . In  $\Omega_m$ , we explore the symmetry of the effective stress tensor; in  $\Omega_f$ , we honor equation (2) and then equation (1) (both the shear stress and the virtual shear strain are transversally uniform within fractures). Subsequently, we substitute in equations (27) and (29). Adopting the Voigt notation leads to

$$\begin{aligned} &\iint_{\Omega^{\text{asy}} \rightarrow \Omega} \eta_{l,k} \sigma'_{kl} d\Omega \\ &= \iint_{\Omega_m} \eta_{l,k} \sigma'_{kl} d\Omega + \iint_{\Omega_f} \eta_{l,k} \sigma'_{kl} d\Omega \\ &= \iint_{\Omega_m} \eta_{(k,l)} \sigma'_{kl} d\Omega + \sum_{i \in n_f} b_{Mi} \int_{\partial f_i} \eta_{\tau_i, n_i} \sigma'_{n_i \tau_i} d\Gamma \\ &= \iint_{\Omega_m} \left\{ \nabla^s \underline{\eta} \right\}^T \mathbf{D}_m \{ \nabla^s \underline{u} \} d\Omega + \sum_{i \in n_f} b_{Mi} \int_{\partial f_i} \nabla_n \eta_{\tau_i} G_{f_i \tau} \nabla_n u_{f_i \tau} d\Gamma \end{aligned} \quad (46)$$

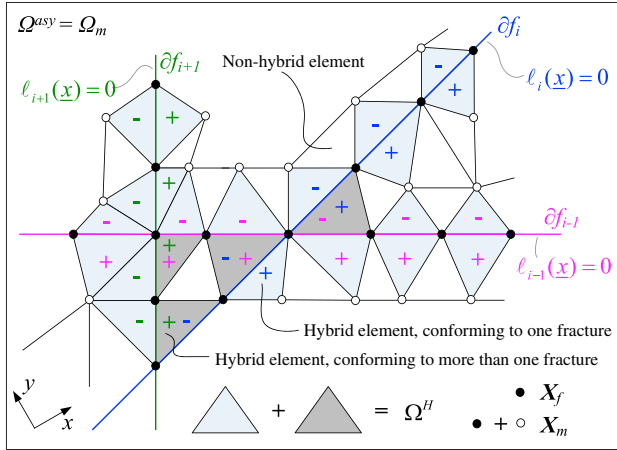


**Figure 7.** Schematic illustration on the discretized model domain. Fractures are discretized as lower dimensional elements tangentially conforming to matrix elements. Any matrix element containing at least one fracture element is a hybrid element, and the rest are nonhybrid elements.

On the RHS, we apply the extended divergence theorem, which leads to

$$\begin{aligned} & \iint_{\Omega^{asy}} (\eta_l \sigma_{kl})_{,k} d\Omega \\ &= \int_{\partial\Omega} \eta_l \sigma_{kl} n_k d\Gamma + \sum_{i \in n_f} \left( \int_{\partial f_i^+} \eta_l \sigma_{kl}^+ n_{f,i,k}^+ d\Gamma + \int_{\partial f_i^-} \eta_l \sigma_{kl}^- n_{f,i,k}^- d\Gamma \right) \quad (47) \\ &= \int_{\partial\Omega} \underline{\eta} \cdot \underline{\sigma} \cdot \underline{n} d\Gamma - \sum_{i \in n_f} \int_{\partial f_i} \underline{\eta} \cdot [|\underline{\sigma}|] \cdot \underline{n}_{f,i} d\Gamma \end{aligned}$$

Substituting equations (46) and (47) into equation (45), exploring symmetry in the remaining term (second term on the LHS of equation (45)), taking into account the traction continuity condition stated in equation (26) and the traction boundary condition equation (34) and recognizing that  $\Omega^{asy} = \Omega_m$ , we arrive at the final weak formulation of the solid problem written in vector form

$$\begin{aligned} & \iint_{\Omega_m} \left\{ \nabla^s \underline{\eta} \right\}^T \mathbf{D}_m \{ \nabla^s \underline{u} \} d\Omega + \sum_{i \in n_f} b_{Mi} \int_{\partial f_i} \nabla_n \eta_{f,i} G_{f,i,\tau} \nabla_n u_{f,i,\tau} d\Gamma \\ & + \iint_{\Omega_m} \left\{ \nabla^s \underline{\eta} \right\}^T \underline{1} ap d\Omega = \int_{\partial\Omega_r} \underline{\eta}^T \underline{t}_h d\Gamma \quad (48) \end{aligned}$$

where  $\eta_{f,i}$  and  $u_{f,i,\tau}$  are the projection of  $\underline{\eta}$  and  $\underline{u}_{f,i}$  on the fracture tangential direction, and  $\underline{1} = [1 \ 1 \ 0]^T$  is the Kronecker delta in vector form.

The LHS of equation (48) includes two additional terms that do not appear in the classic weak form of the force balance equation: the second term accounts for the fracture zone constitutive behavior, and the third term accounts for the poroelastic effect.

## 4. Discretization

### 4.1. Space Discretization and Hybrid Elements

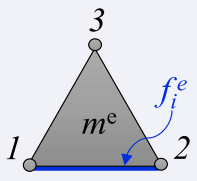
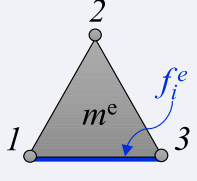
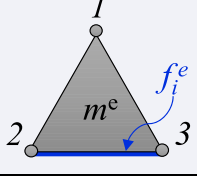
Recall that  $p_{f,i}(\underline{x}, t) \subset p_m(\underline{x}, t) = p(\underline{x}, t)$  and  $\underline{u}_{f,i}(\underline{x}, t) \subset \underline{u}_m(\underline{x}, t) = \underline{u}(\underline{x}, t)$  in  $\Omega^{asy}$ . Accordingly, we spatially discretize  $\Omega^{asy}$  into a set of linear elements such that each lower dimensional linear fracture  $\partial f_i$  ( $i = 1 \sim n_f$ ) tangentially conforms to the edges of a subset of these elements (see Figure 7). Denote the matrix node set as  $\mathbf{X}_m$  and fracture node set as  $\mathbf{X}_f$ , then  $\mathbf{X}_f \subset \mathbf{X}_m$ . Fracture nodes thus hold no additional degrees of freedom but share values with matrix nodes, which ensures the continuity of pressure and displacements. The elements that fractures conform to are referred to as “hybrid elements” in this study. They contain at least two fracture nodes from the same fracture and constitute a hybrid domain  $\Omega^H, \Omega^H \subset \Omega^{asy}$ . The  $\Omega^H$  associated with  $\partial f_i$  will be referred to as  $\Omega^{H_i}$ , which is composed of  $\Omega^{H_i^+}$  on the positive side and  $\Omega^{H_i^-}$  on the negative side. Suppose  $\partial f_i$  lies on the line  $l_i(\underline{x}) = ax - y + c = 0$ .  $l_i(\underline{x}) > 0 \forall \underline{x} \in \Omega^{H_i^+}, l_i(\underline{x}) < 0 \forall \underline{x} \in \Omega^{H_i^-}$ .

We have chosen the fluid pressure  $p$  and the solid displacement  $\underline{u}$  as the primary unknowns. For a hybrid element conforming to  $\partial f_i$ , we denote the nodal pressure as  $\hat{\zeta}_m^H$  and  $\hat{\zeta}_{f,i}^H$  and the nodal displacements as  $\underline{d}_m^H$  and  $\underline{d}_{f,i}^H$ .  $\hat{\zeta}_{f,i}^H \subset \hat{\zeta}_m^H, \underline{d}_{f,i}^H \subset \underline{d}_m^H$ . We then define two “dimensional transformation matrices” associated with  $\partial f_i$ ,  $\mathbf{Q}_{f,i}$  and  $\mathbf{L}_{f,i}$ , for the fluid problem and the solid problem, respectively, such that

$$\begin{aligned} \hat{\zeta}_{f,i}^H &= \mathbf{Q}_{f,i} \hat{\zeta}_m^H \\ \underline{d}_{f,i}^H &= \mathbf{L}_{f,i} \underline{d}_m^H \quad (49) \end{aligned}$$

Here  $\mathbf{Q}$  and  $\mathbf{L}$  are composed of 0 and 1, and  $\mathbf{Q}_{f,i} \mathbf{Q}_{f,i}^T = 1, \mathbf{L}_{f,i} \mathbf{L}_{f,i}^T = 1$ .

**Table 1**  
Example of Element-Wise Dimensional Transformation Matrices for Linear Triangular Hybrid Elements

Local node number in a hybrid element	$\mathbf{Q}_{f_i}$	$\mathbf{L}_{f_i}$
	$\begin{bmatrix} 1 & 0 & 0 \\ 0 & 1 & 0 \end{bmatrix}$	$\begin{bmatrix} 1 & 0 & 0 & 0 & 0 & 0 \\ 0 & 1 & 0 & 0 & 0 & 0 \\ 0 & 0 & 1 & 0 & 0 & 0 \\ 0 & 0 & 0 & 1 & 0 & 0 \end{bmatrix}$
	$\begin{bmatrix} 1 & 0 & 0 \\ 0 & 0 & 1 \end{bmatrix}$	$\begin{bmatrix} 1 & 0 & 0 & 0 & 0 & 0 \\ 0 & 1 & 0 & 0 & 0 & 0 \\ 0 & 0 & 0 & 0 & 1 & 0 \\ 0 & 0 & 0 & 0 & 0 & 1 \end{bmatrix}$
	$\begin{bmatrix} 0 & 1 & 0 \\ 0 & 0 & 1 \end{bmatrix}$	$\begin{bmatrix} 0 & 0 & 1 & 0 & 0 & 0 \\ 0 & 0 & 0 & 1 & 0 & 0 \\ 0 & 0 & 0 & 0 & 1 & 0 \\ 0 & 0 & 0 & 0 & 0 & 1 \end{bmatrix}$

For example, for a linear triangular element,  $\hat{\zeta}_m^H = (\zeta_{m1}^H, \zeta_{m2}^H, \zeta_{m3}^H)^T$ , and  $\underline{d}_m^H = (d_{m1x}^H, d_{m1y}^H, d_{m2x}^H, d_{m2y}^H, d_{m3x}^H, d_{m3y}^H)^T$ . Accordingly, the element-wise  $\mathbf{Q}_{f_i}$  and  $\mathbf{L}_{f_i}$  take the following different forms, depending on the local node number of the matrix element  $m^e$  in relation to the fracture line elements  $f_i^e$  (see Table 1):

We denote the shape functions associated with  $m^e$  and the conforming  $f_i^e$  as  $\underline{N}_m$  and  $\underline{N}_{f_i\tau}$  for the fluid problem, and as  $\mathbf{N}_m$  and  $\mathbf{N}_{f_i\tau}$  for the solid problem.  $\underline{N}_m$  and  $\mathbf{N}_m$  are defined in  $\underline{x}$ , while  $\underline{N}_{f_i\tau}$  and  $\mathbf{N}_{f_i\tau}$  are defined along the fracture tangential direction  $\tau_{f_i}$ . They take the following forms:

$$\underline{N}_m = (N_{m1}(\underline{x}), N_{m2}(\underline{x}), N_{m3}(\underline{x})) \quad (50)$$

$$\underline{N}_{f_i\tau} = (N_{f_i\tau 1}, N_{f_i\tau 2}) \quad (51)$$

$$\mathbf{N}_m = \begin{bmatrix} N_{m1}(\underline{x}) & 0 & N_{m2}(\underline{x}) & 0 & N_{m3}(\underline{x}) & 0 \\ 0 & N_{m1}(\underline{x}) & 0 & N_{m2}(\underline{x}) & 0 & N_{m3}(\underline{x}) \end{bmatrix} \quad (52)$$

$$\mathbf{N}_{f_i\tau} = \begin{bmatrix} N_{f_i\tau 1} & 0 & N_{f_i\tau 2} & 0 \\ 0 & N_{f_i\tau 1} & 0 & N_{f_i\tau 2} \end{bmatrix} \quad (53)$$

For linear 2-D and 1-D elements, one can verify the validity of the following relationships, which will soon prove useful:

$$\underline{N}_m|_{\partial f_i} = \underline{N}_{f_i\tau} \mathbf{Q}_{f_i}, \text{ or } \int_{\partial f_i} \underline{N}_m^T(\cdot) d\Gamma = \int_{\partial f_i} \mathbf{Q}_{f_i}^T \underline{N}_{f_i\tau}^T(\cdot) d\Gamma \quad (54)$$

$$\mathbf{N}_m|_{\partial f_i} = \mathbf{N}_{f_i\tau} \mathbf{L}_{f_i}, \text{ or } \int_{\partial f_i} \mathbf{N}_m^T(\cdot) d\Gamma = \int_{\partial f_i} \mathbf{L}_{f_i}^T \mathbf{N}_{f_i\tau}^T(\cdot) d\Gamma \quad (55)$$

#### 4.2. Hybrid-Dimensional, Equal-Order, Mixed Finite Element Interpolation

Similar to what is commonly used in a fracture-free coupled poromechanical problem, here, we adopt the classical two-field mixed finite element method, in which the two coupled primary unknowns,  $p$  and  $\underline{u}$ , are interpolated over the same finite element (e.g., Korsawe et al., 2006; White & Borja, 2011). Furthermore, it is well known that for a drained coupled system, as is the focus of this study, the equal-low-order interpolation pair well satisfies the so-called inf-sup constraint, known also as the Ladyženskaja-Babuška-Brezzi condition, and therefore, no instability in the fluid pressure field will arise (e.g., Choo & Borja, 2015). This enables us to utilize the same discrete space for interpolation. However, in contrast to a standard equal-dimensional interpolation scheme, here, the hybrid element described in section 4.1 naturally calls for hybrid-dimensional interpolation of the primary unknowns. Specifically, in fracture-related terms,  $p$  and  $\underline{u}$  will be interpolated in 1-D using fracture nodes only, whereas in other terms, they will be interpolated in 2-D using matrix nodes. Meanwhile, the two test functions will always be interpolated in 2-D using matrix nodes for maintaining consistency on both sides of the equation. This will lead to a mismatch in the size of the resulting matrix form; however, this mismatch can be reconciled using the dimensional transformation matrices defined above together with equations (54) and (55). This ensures that the same primary unknown vector will be gathered from all terms on the LHS, and the same arbitrary vector will be canceled on both sides. For a nonhybrid element, standard 2-D interpolation is employed. For brevity, we will not distinguish between hybrid and nonhybrid elements and will omit writing the superscript "H," e.g.,  $\hat{\zeta}_m^H$  as  $\hat{\zeta}_m$ . In addition, a subscript "g" will be used to indicate a quantity associated with an element in contact with or a node on the Dirichlet boundary. We note that prior to interpolation, hybrid elements associated with  $\partial f_i$  ( $i = 1 \sim n_f$ ) can be identified. The details of the interpolation are given below.

#### 4.2.1. The Fluid Problem With Solid-to-Fluid Coupling

The interpolation of the fluid pressure and its local time derivative is hybrid-dimensional. Employing the Galerkin approximation on the fluid Dirichlet boundary, we have

$$p \approx \underline{N}_m \hat{c}_m + \underline{N}_g \hat{c}_g, \dot{p} \approx \underline{N}_m \dot{\hat{c}}_m + \underline{N}_g \dot{\hat{c}}_g \quad \forall \underline{x} \in \Omega_m \quad (56)$$

$$p \approx \underline{N}_{f_i \tau} \hat{c}_{f_i} = \underline{N}_{f_i \tau} \mathbf{Q}_{f_i} \hat{c}_m, \dot{p} \approx \underline{N}_{f_i \tau} \dot{\hat{c}}_{f_i} = \underline{N}_{f_i \tau} \mathbf{Q}_{f_i} \dot{\hat{c}}_m \quad \forall \underline{x} \in \partial f_i \quad (57)$$

Taking advantage of the constant element-wise fluid flux associated with linear elements, the flow velocity discontinuity in equation (42) can be interpolated as

$$-[[\kappa_m \nabla p_m]] \approx - \left( \kappa_m^+ \nabla \underline{N}_m^+ \hat{c}_m^+ - \kappa_m^- \nabla \underline{N}_m^- \hat{c}_m^- \right) \quad \forall \underline{x} \in \Omega^H \quad (58)$$

Because fractures act as sources only for shear deformation and the volumetric deformation is only due to the matrix, it is therefore adequate to interpolate the volumetric strain rate of the medium simply using the matrix nodes. Here we adopt the following standard Galerkin form:

$$\nabla \cdot \underline{\dot{u}} \approx \underline{b}_m \dot{\underline{d}}_m + \underline{b}_g \dot{\underline{d}}_g \quad (59)$$

Here for a 2-D problem,  $\underline{b}_m$  takes the following form:

$$\underline{b}_m = \underline{1}^T \mathbf{B}_m = \nabla^T \mathbf{N}_m \quad (60)$$

where  $\mathbf{B}_m$  is given in the following section by equation (63).

Lastly, the weighting function can be interpolated in 2-D using matrix nodes:

$$w \approx \underline{N}_m \hat{c}_m \quad (61)$$

where  $\hat{c}_m$  is an arbitrary vector or virtual nodal pressure.

#### 4.2.2. The Solid Problem With Fluid-to-Solid Coupling

Following standard methods, the test function, the virtual strain, and the strain can be interpolated in 2-D using matrix nodes. Employing the Galerkin approximation on the solid Dirichlet boundary, we have

$$\underline{\eta} \approx \mathbf{N}_m \underline{\varphi}_m \quad \left\{ \nabla^s \underline{\eta} \right\} \approx \mathbf{B}_m \underline{\varphi}_m \quad \left\{ \nabla^s \underline{u} \right\} \approx \mathbf{B}_m \underline{d}_m + \mathbf{B}_g \underline{d}_g \quad \forall \underline{x} \in \Omega_m \quad (62)$$

where  $\underline{\varphi}_m$  is an arbitrary vector or virtual nodal displacement and  $\mathbf{B}$  is the standard displacement–strain transformation matrix, which reads

$$\mathbf{B}_m = \begin{bmatrix} N_{m1,x} & 0 & N_{m2,x} & 0 & N_{m3,x} & 0 \\ 0 & N_{m1,y} & 0 & N_{m2,y} & 0 & N_{m3,y} \\ N_{m1,y} & N_{m1,x} & N_{m2,y} & N_{m2,x} & N_{m3,y} & N_{m3,x} \end{bmatrix} \quad (63)$$

The projections of  $\underline{\eta}$  along a fracture is specified as

$$\eta_{\tau_i} = \underline{\tau}_i \cdot \underline{\eta} = \underline{\tau}_i^T \underline{\eta} = \underline{\tau}_i^T \mathbf{N}_m \underline{\varphi}_m = \underline{\varphi}_m^T \mathbf{N}_m^T \underline{\tau}_i \quad \forall \underline{x} \in \partial f_i \quad (64)$$

where

$$\underline{\tau}_i = (\cos \theta_i, \sin \theta_i)^T \quad (65)$$

1-D interpolation is then employed for the fracture tangential displacement:

$$u_{f_i \tau} \approx \underline{N}_{f_i \tau} \underline{d}_{f_i \tau} = \underline{N}_{f_i \tau} \mathbf{R}_{f_i} \underline{d}_{f_i} = \underline{N}_{f_i \tau} \mathbf{R}_{f_i} \mathbf{L}_{f_i} \underline{d}_m \quad \forall \underline{x} \in \partial f_i \quad (66)$$

where  $\mathbf{R}_{f_i}$  is the rotation matrix dependent on the fracture orientation:

$$\mathbf{R}_{f_i} = \begin{bmatrix} \cos \theta_i & \sin \theta_i & 0 & 0 \\ 0 & 0 & \cos \theta_i & \sin \theta_i \end{bmatrix} \quad (67)$$

From equations (51), (53), (65), and (67), it follows that

$$\mathbf{N}_{f_i \tau}^T \underline{\tau}_i = (\underline{N}_{f_i \tau} \mathbf{R}_{f_i})^T = \mathbf{R}_{f_i}^T \underline{N}_{f_i \tau}^T \quad (68)$$



Substituting in equations (64) and (66), honoring equation (55), and consulting equation (68), we arrive at the following symmetric form of the fracture-related term in equation (48):

$$\begin{aligned}
 \sum_{i \in n_f} b_{Mi} \int_{\partial f_i} \nabla n \mathbf{N}_{f_i \tau} \mathbf{G}_{f_i \tau} \nabla n \mathbf{u}_{f_i \tau} d\Gamma &= \sum_{i \in n_f} b_{Mi} \int_{\partial f_i} \phi_m^T \mathbf{N}_{m, n_{f_i}}^T \mathbf{I}_{f_i} \mathbf{G}_{f_i \tau} \mathbf{N}_{f_i \tau, n_{f_i}} \mathbf{R}_{f_i} \mathbf{L}_{f_i} d\Gamma \underline{d}_m \\
 &= \sum_{i \in n_f} b_{Mi} \int_{\partial f_i} \phi_m^T \mathbf{L}_{f_i}^T \mathbf{N}_{f_i \tau, n_{f_i}}^T \mathbf{I}_{f_i} \mathbf{G}_{f_i \tau} \mathbf{N}_{f_i \tau, n_{f_i}} \mathbf{R}_{f_i} \mathbf{L}_{f_i} d\Gamma \underline{d}_m \\
 &= \sum_{i \in n_f} b_{Mi} \int_{\partial f_i} \phi_m^T \mathbf{L}_{f_i}^T \mathbf{R}_{f_i}^T \mathbf{N}_{f_i \tau, n_{f_i}}^T \mathbf{G}_{f_i \tau} \mathbf{N}_{f_i \tau, n_{f_i}} \mathbf{R}_{f_i} \mathbf{L}_{f_i} d\Gamma \underline{d}_m
 \end{aligned} \quad (69)$$

Here the normal gradient of  $\mathbf{N}_{f_i \tau}$  is approximated as the following, based on the normal transversal uniformity assumption (here we give the element-wise expression):

$$\nabla n \mathbf{N}_{f_i \tau}^e = \mathbf{N}_{f_i \tau, n_{f_i}}^e = \mathbf{N}_{f_i \tau, \tau_{f_i}}^e \tau_{f_i, n_{f_i}} = \begin{pmatrix} -\frac{1}{l_i^e} & \frac{1}{l_i^e} \\ \frac{1}{l_i^e} & \frac{1}{l_i^e} \end{pmatrix} \frac{l_i^e}{b_{Mi}} = \begin{pmatrix} -\frac{1}{b_{Mi}} & \frac{1}{b_{Mi}} \\ \frac{1}{b_{Mi}} & \frac{1}{b_{Mi}} \end{pmatrix} \quad (70)$$

where  $l_i^e$  is the length of a line element of the  $i$ th fracture.

### 4.3. Semidiscrete Form

Substituting equations (56)–(61) into equation (44); substituting equations (56), (62), (64), (66), and (69)–(70) into equation (48); and noticing equations (19), (54), and (55), we arrive at the following semidiscrete form of the nonlinear and coupled equations:

$$\begin{bmatrix} \mathbf{M}(\hat{\zeta}_f) & -\mathbf{C}^T \\ \mathbf{0} & \mathbf{0} \end{bmatrix} \begin{Bmatrix} \hat{\zeta}_m \\ \underline{d}_m \end{Bmatrix} + \begin{bmatrix} \mathbf{K}(\hat{\zeta}_f) & \mathbf{0} \\ \mathbf{C} & \mathbf{G} \end{bmatrix} \begin{Bmatrix} \hat{\zeta}_m \\ \underline{d}_m \end{Bmatrix} = \begin{Bmatrix} \underline{F} \\ \underline{Y} \end{Bmatrix} \quad (71)$$

where  $\hat{\zeta}_f = \cup_{i=1}^{n_f} \hat{\zeta}_{f_i} \subset \hat{\zeta}_m$ , and the matrices and vectors take the following forms:

$$\begin{aligned}
 \mathbf{M}(\hat{\zeta}_f) &= \underbrace{\iint_{\Omega_m} \mathbf{N}_m^T (\Lambda_0 \phi_{m0} (C_m + C_\rho)) \mathbf{N}_m d\Omega}_{\text{matrix storage capacity, } \mathbf{M}_m} \\
 &+ \underbrace{\sum_{i \in n_f} b_{Hi}(\hat{\zeta}_{f_i}) \int_{\partial f_i} \mathbf{Q}_{f_i}^T \mathbf{N}_{f_i \tau}^T ((1 - \Lambda_0) \phi_{f_i0} (C_{f_i} + C_\rho)) \mathbf{N}_{f_i \tau} \mathbf{Q}_{f_i} d\Gamma}_{\text{DFN storage capacity, } \sum_i \mathbf{M}_{f_i}(\hat{\zeta}_{f_i})}
 \end{aligned} \quad (72)$$

$$\begin{aligned}
 \mathbf{K}(\hat{\zeta}_f) &= \underbrace{\iint_{\Omega_m} (\nabla \mathbf{N}_m)^T \mathbf{k}_m (\nabla \mathbf{N}_m) d\Omega}_{\text{matrix conductivity, } \mathbf{K}_m} \\
 &+ \underbrace{\sum_{i \in n_f} b_{Hi}(\hat{\zeta}_{f_i}) \int_{\partial f_i} \mathbf{Q}_{f_i}^T (\nabla_\tau \mathbf{N}_{f_i \tau})^T \left( \frac{1}{12} b_{Hi}^2(\hat{\zeta}_{f_i}) \right) (\nabla_\tau \mathbf{N}_{f_i \tau}) \mathbf{Q}_{f_i} d\Gamma}_{\text{DFN tangential conductivity, } \sum_i \mathbf{K}_{f_i}(\hat{\zeta}_{f_i})} \\
 &- \underbrace{\sum_{j \in n_f} \int_{\partial f_j} \mathbf{Q}_{f_j}^T \mathbf{N}_{f_j \tau}^T \left( \frac{1}{12} b_{Hj}^2(\hat{\zeta}_{f_j}) \right) \nabla_\tau \mathbf{N}_{f_j \tau} \mathbf{Q}_{f_j} d\Gamma}_{\text{matrix-to-DFN mass transferability, } -\sum_j \mathbf{K}_{m_{f_j}}(\hat{\zeta}_{f_j})} \\
 &+ \underbrace{\sum_{k \in n_{fl}} \int_{\partial f_k} \mathbf{Q}_{f_k}^T \mathbf{N}_{f_k \tau}^T n_{f_k}^T (\mathbf{k}_m^+ \nabla \mathbf{N}_m^+ - \mathbf{k}_m^- \nabla \mathbf{N}_m^-) d\Gamma}_{\text{DFN-to-matrix mass transferability, } \sum_k \mathbf{K}_{f_k m}}
 \end{aligned} \quad (73)$$

$$\mathbf{G} = \underbrace{\iint_{\Omega_m} \mathbf{B}_m^T \mathbf{D}_m \mathbf{B}_m d\Omega}_{\text{matrix stiffness, } \mathbf{G}_m} + \underbrace{\sum_{i \in n_f} b_{Mi} \int_{\partial f_i} \mathbf{L}_{f_i}^T \mathbf{R}_{f_i}^T (\nabla n \mathbf{N}_{f_i \tau})^T \mathbf{G}_{f_i \tau} (\nabla n \mathbf{N}_{f_i \tau}) \mathbf{R}_{f_i} \mathbf{L}_{f_i} d\Gamma}_{\text{DFN tangential stiffness, } \sum_i \mathbf{G}_{f_i}} \quad (74)$$

$$\mathbf{c} = \underbrace{\iint_{\Omega_m} \mathbf{N}_m^T \alpha \nabla N_m d\Omega}_{\text{coupling matrix, DFN-independent}} \quad (75)$$

$$\begin{aligned} \underline{F} = & \underbrace{\iint_{\partial\Omega_f} \mathbf{N}_m^T v_h d\Gamma}_{\text{fluid Neumann B.C.}} + \underbrace{\iint_{\Omega_m} \mathbf{N}_m^T s d\Omega}_{\text{external fluid source}} \quad (76) \\ & - \underbrace{\left( \iint_{\Omega_m} (\nabla N_m)^T \mathbf{K}_m (\nabla N_g) \hat{\zeta}_g d\Omega + \iint_{\Omega_m} \mathbf{N}_m^T (\Lambda_0 \phi_{m0} C_m) N_g \hat{\zeta}_g d\Omega \right)}_{\text{fluid Dirichlet B.C.}} \\ & - \underbrace{\iint_{\Omega_m} \mathbf{N}_m^T \alpha \nabla^T \mathbf{N}_g \dot{d}_g d\Omega}_{\text{coupling at the Solid Dirichlet boundary}} \end{aligned}$$

$$\underline{Y} = \underbrace{\int_{\partial\Omega_f} \mathbf{N}_m^T \underline{t}_h d\Gamma}_{\text{solid Neumann B.C.}} - \underbrace{\iint_{\Omega_m} \mathbf{B}_m^T \mathbf{D}_m \mathbf{B}_g \dot{d}_g d\Omega}_{\text{solid Dirichlet B.C.}} - \underbrace{\iint_{\Omega_m} \mathbf{N}_m^T \alpha \nabla N_g \hat{\zeta}_g d\Omega}_{\text{coupling at the fluid Dirichlet boundary}} \quad (77)$$

When compared to the known semidiscrete form of equation for a classical linear and fracture-free poromechanical problem, equations (72)–(77) highlight a DFN's threefold effect. The first effect is reflected by the modification to two existing terms, specifically, the first term in  $\mathbf{M}$  and the last term in  $\underline{F}$ , where the geometry-dependent parameter  $\Lambda_0(\underline{x})$  appears. It eliminates the need for calculating upscaled hydraulic properties as are required by the DPDP model.  $\underline{F}$  is otherwise canonical owing to the assumption that the external fluid source is provided only in the matrix, and possible interactions at fracture-boundary intersections are not considered.

The second effect is shown by several additional terms, as elaborated here. In  $\mathbf{M}$ , the second term arises from fractures acting as a primary type of pores for fluid storage. In  $\mathbf{K}$ , the second term arises from the fracture tangential flow. This term, although in different forms, has also been shown in several other studies (Baca et al., 1984; Kim & Deo, 2000; Yao et al., 2010; Zhang et al., 2013). These two terms directly result from mass conservation over the fracture domain that does not interact with the matrix domain. The interaction (mass exchange) is introduced by the next two terms. The third term in  $\mathbf{K}$  applies only to fully immersed fractures where matrix-to-fracture mass transfer occurs, and the fourth term in  $\mathbf{K}$ , which introduces asymmetry and applies only to partially immersed fractures, accounts for fracture-to-matrix mass transfer. The two transfer terms, together with the geometry-dependent parameter  $\Lambda_0(\underline{x})$ , allow formulation of the conservation law over an integrated matrix-fracture domain; this contrasts with the domain separation approach favored by the DPDP model. In addition, the two transfer terms are especially important for studying the role of poroelastic stress in induced seismicity as they predict an equivalent body force acting away or toward fractures. We also note that all the terms in  $\mathbf{M}$  and  $\mathbf{K}$  distinguish our method from a single-layer interface element approach developed for such a weakly discontinuous flow problem where the mass exchange between fractures and the matrix is assumed and the storage capacity of the system is not considered (Segura & Carol, 2004). Finally, in  $\mathbf{G}$ , the second term is due to the fact that fractures act as finite-thickness deformation zones even prior to failure.

Element-wise, all the fracture-related terms appear only for hybrid elements and vanish for nonhybrid elements. This allows for the development of an independent subroutine for bringing the DFN into the existing computational framework of poromechanics. The standard procedure for assembling global matrices still applies. It is worth noting that prior to the assembly, the elemental matrices corresponding to the second term in  $\mathbf{M}$ , the second and third terms in  $\mathbf{K}$ , and the second term in  $\mathbf{G}$  all need to be halved to prevent repeated collection of contributions from fracture elements. Note also that at an elemental level, the sums in these terms are only intended over however many fractures a hybrid element conforms to.

The third effect lies in the nonlinearity that is introduced into the system by equations (72) and (73) via the pressure-dependent hydraulic aperture. It is obtained by replacing the pressure in equation (21) with the

corresponding discrete nodal pressure. Finally, notice that the coupling matrix is not dependent on the DFN. Details regarding the implementation of the DFN is given in Appendix A.3.

#### 4.4. Time Discretization

The solution to equation (71) is advanced in time in a fully coupled manner using a fully implicit finite difference method (the backward Euler scheme), which offers unconditional stability and first-order accuracy. Evaluating all pressure-dependent terms and the external nodal force vector at the next time step, we obtain

$$\begin{bmatrix} \mathbf{M}^{(n+1)} & -\mathbf{C}^T \\ \mathbf{0} & \mathbf{0} \end{bmatrix} \frac{1}{dt} \left\{ \begin{Bmatrix} \hat{\zeta}_m \\ \underline{d}_m \end{Bmatrix}^{(n+1)} - \begin{Bmatrix} \hat{\zeta}_m \\ \underline{d}_m \end{Bmatrix}^{(n)} \right\} + \begin{bmatrix} \mathbf{K}^{(n+1)} & \mathbf{0} \\ \mathbf{C} & \mathbf{G} \end{bmatrix} \begin{Bmatrix} \hat{\zeta}_m \\ \underline{d}_m \end{Bmatrix}^{(n+1)} \approx \begin{Bmatrix} \underline{F} \\ \underline{Y} \end{Bmatrix}^{(n+1)} \quad (78)$$

where  $dt$  is the time increment which, in theory, is not subjected to any restriction and superscripts  $(n+1)$  and  $(n)$  indicate the next and the current time steps.

#### 5. Linearization

To start, we divide both sides of the solid subproblem by  $dt$  and rewrite equation (78) in the following form:

$$\begin{bmatrix} \mathbf{M}^{(n+1)} & -\mathbf{C}^T \\ \mathbf{0} & \mathbf{0} \end{bmatrix} \frac{1}{dt} \left\{ \begin{Bmatrix} \hat{\zeta}_m \\ \underline{d}_m \end{Bmatrix}^{(n+1)} - \begin{Bmatrix} \hat{\zeta}_m \\ \underline{d}_m \end{Bmatrix}^{(n)} \right\} + \begin{bmatrix} \mathbf{K}^{(n+1)} & \mathbf{0} \\ \mathbf{C}/dt & \mathbf{G}/dt \end{bmatrix} \begin{Bmatrix} \hat{\zeta}_m \\ \underline{d}_m \end{Bmatrix}^{(n+1)} \approx \begin{Bmatrix} \underline{F}^{(n+1)} \\ \underline{Y}^{(n+1)}/dt \end{Bmatrix} \quad (79)$$

As will be shown, this additional step ensures the positive-definiteness of the Jacobian (see equation (85)) irrespective of the choice of  $dt$ , provided that the capacity, conductivity, and stiffness matrices (see equations (72)–(74)) are positive-definite. Equation (79) is nonlinear and must be solved using an iterative linearized procedure. Here we implement the classic Newton-Raphson scheme:

$$\mathbf{J}(\underline{\zeta}^{(n+1,k)}, dt) (\underline{\zeta}^{(n+1,k+1)} - \underline{\zeta}^{(n+1,k)}) = -\underline{R}(\underline{\zeta}^{(n+1,k)}, \underline{\zeta}^{(n)}, dt) \quad (80)$$

where  $\mathbf{J}$  is the Jacobian,  $\underline{R}$  is the residual, and  $\underline{\zeta} = [\hat{\zeta}_m, \underline{d}_m]^T$  is the primary unknown, all of which are evaluated at the time step  $(n+1)$ , and  $(k+1)$  and  $(k)$  indicate two successive iteration steps.

The residual  $\underline{R}$  is obtained from equation (79) by multiplying both sides with  $dt$  and rearranging it as the following:

$$\begin{aligned} \underline{R}^{(n+1,k)} &= \begin{Bmatrix} \underline{R}_f \\ \underline{R}_y \end{Bmatrix}^{(n+1,k)} \\ &= \begin{bmatrix} \mathbf{M}^{(n+1,k)} + dt\mathbf{K}^{(n+1,k)} & -\mathbf{C}^T \\ \mathbf{C} & \mathbf{G} \end{bmatrix} \begin{Bmatrix} \hat{\zeta}_m \\ \underline{d}_m \end{Bmatrix}^{(n+1,k)} - \begin{bmatrix} \mathbf{M}^{(n+1,k)} & -\mathbf{C}^T \\ \mathbf{0} & \mathbf{0} \end{bmatrix} \begin{Bmatrix} \hat{\zeta}_m \\ \underline{d}_m \end{Bmatrix}^{(n)} - \begin{Bmatrix} dt\underline{F}^{(n+1)} \\ \underline{Y}^{(n+1)} \end{Bmatrix} \end{aligned} \quad (81)$$

Here

$$\mathbf{M}^{(n+1,k)} = \mathbf{M}_m + \sum_{i \in n_f} a_i^{(n+1,k)} \mathbf{M}_{f_i}^{(0)} \quad (82)$$

$$\mathbf{K}^{(n+1,k)} = \mathbf{K}_m + \sum_{i \in n_f} (a_i^{(n+1,k)})^3 \mathbf{K}_{f_i}^{(0)} - \sum_{j \in n_f} (a_j^{(n+1,k)})^2 \mathbf{K}_{mf_j}^{(0)} + \sum_{k \in n_m} \mathbf{K}_{f_{km}} \quad (83)$$

In equations (82) and (83),  $\mathbf{M}_{f_i}^{(0)}$ ,  $\mathbf{K}_{f_i}^{(0)}$ , and  $\mathbf{K}_{mf_j}^{(0)}$  are obtained from their respective expressions shown in equations (72) and (73) by substituting in the corresponding initial hydraulic aperture, and the dimensionless parameter  $a$ , evaluated at the time step  $(n+1)$  and the nonlinear iteration step  $(k)$ , is given by

$$a_r^{(n+1,k)} = \left( 1 + C_{f_r} \hat{\zeta}_{f_r}^{(n+1,k)} \right), r = i, j \quad (84)$$

Lastly, the Jacobian  $\mathbf{J}$  takes the form of

$$\mathbf{J} = \begin{bmatrix} \mathbf{J}_{11} & \mathbf{J}_{12} \\ \mathbf{J}_{21} & \mathbf{J}_{22} \end{bmatrix}^{(n+1,k)} = \begin{bmatrix} \mathbf{J}_{11}^{(n+1,k)} & \mathbf{J}_{12} \\ \mathbf{J}_{21} & \mathbf{J}_{22} \end{bmatrix} \quad (85)$$

where the four block submatrices are derived from equation (81) and they read

$$\mathbf{J}_{11} = \frac{\partial \mathbf{R}_F^{(n+1,k)}}{\partial \hat{\zeta}_m^{(n+1,k)}} = \mathbf{M}_m + \sum_{i \in n_f} \left( a_i^{(n+1,k)} + C_{f_i} \hat{\zeta}_{f_i}^{(n+1,k)} \right) \mathbf{M}_{f_i}^{(0)} \quad (86)$$

$$+ dt \left( \mathbf{K}_m + \sum_{i \in n_f} \left( \left( a_i^{(n+1,k)} \right)^3 + 3 \left( a_i^{(n+1,k)} \right)^2 C_{f_i} \hat{\zeta}_{f_i}^{(n+1,k)} \right) \mathbf{K}_{f_i}^{(0)} \right)$$

$$+ dt \left( - \sum_{j \in n_{\eta}} \left( \left( a_j^{(n+1,k)} \right)^2 + 2 a_j^{(n+1,k)} C_{f_j} \hat{\zeta}_{f_j}^{(n+1,k)} \right) \mathbf{K}_{mf_j}^{(0)} + \sum_{k \in n_{\eta}} \mathbf{K}_{f_k m} \right)$$

$$\mathbf{J}_{12} = \frac{\partial \mathbf{R}_F^{(n+1,k)}}{\partial \underline{d}_m^{(n+1,k)}} = -\mathbf{C}^T \quad (87)$$

$$\mathbf{J}_{21} = \frac{\partial \mathbf{R}_Y^{(n+1,k)}}{\partial \hat{\zeta}_m^{(n+1,k)}} = \mathbf{C} \quad (88)$$

$$\mathbf{J}_{22} = \frac{\partial \mathbf{R}_Y^{(n+1,k)}}{\partial \underline{d}_m^{(n+1,k)}} = \mathbf{G} = \mathbf{G}_m + \sum_{i \in n_f} \mathbf{G}_{f_i} \quad (89)$$

## 6. Numerical Example

### 6.1. Asymptotic Model Setup

We generate a 2-D asymptotic model domain containing a stochastic DFN composed of 100 1-D fractures (see Figure 8). The domain is 200 m  $\times$  200 m and contains a centered circular empty area with radius 5 m. Dirichlet and Neumann boundaries are indicated. In this example,  $\partial\Omega_p = \partial\Omega_u$  and  $\partial\Omega_v = \partial\Omega_t$ . Centers of fracture are seeded following a nonuniform random distribution and are more concentrated near the domain center. Fracture lengths and orientations are generated following uniform distributions on the ranges [20 m, 50 m] and  $[0^\circ, 360^\circ]$ , respectively. The DFN is partially interconnected. Type I and II fractures are colored with blue and green, respectively. Several meshing tools are available for generating the conforming mesh (e.g., Erhel et al., 2009; Hyman et al., 2015) required by this study. Here we augment an open-source MATLAB code called DistMesh (Persson & Strang, 2004). Without elaborating on its meshing algorithm, here, we link it to our stochastic DFN by (1) iteratively defining an appropriate “edge” function based on the supplied geometry of each fracture, (2) setting global mesh size and quality control parameters for all fractures, and (3) specifying densely spaced fixed points on each fracture. The asymptotic model domain is then discretized into a set of linear triangular elements at a specified resolution, and fractures are resolved as conforming linear line elements. The final representation of the DFN might be slightly different, but an excellent preservation of the DFN is always maintained with a high-quality mesh. Hybrid elements are then identified (Appendix A.3) and are highlighted in magenta.

Table 2 lists the nominal parameters used in the numerical example. For demonstration purposes, and this does not change the generality of the method, we let all fractures have the same hydraulic and mechanical properties. We simulate injection by imposing a constant pressure of 5 MPa on  $\partial\Omega_p$  instead of by prescribing fluid flux or specifying external sources. The simulated total injection time is 100 min, and the time increment is set to be 100 s.

Equation (78) is solved following the iterative linearization procedure described in section 5. Within each time step, the iteration is terminated when the following criteria are met:

$$\| \mathbf{R}(\underline{\zeta}^{n+1,k+1}) \|_2 \leq 10^{-6} \quad \left\| \hat{\zeta}_m^{n+1,k+1} - \hat{\zeta}_m^{n+1,k} \right\|_2 \leq 0.01 \left\| \hat{\zeta}_m^n \right\|_2 \quad \left\| \underline{d}_m^{n+1,k+1} - \underline{d}_m^{n+1,k} \right\|_2 \leq 0.01 \left\| \underline{d}_m^n \right\|_2 \quad (90)$$

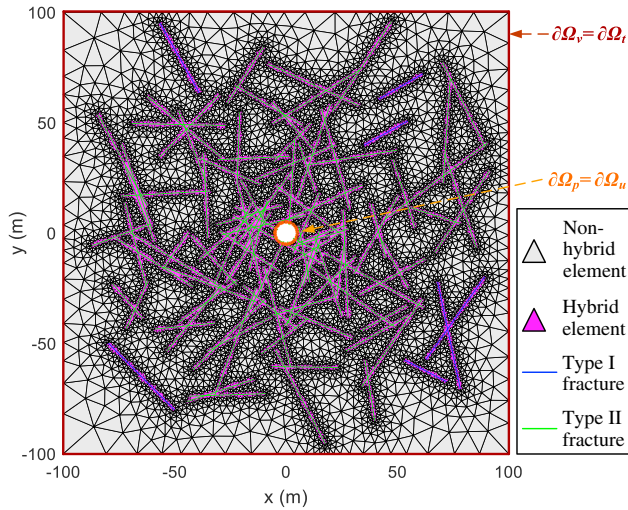


**Figure 8.** A 2-D asymptotic model domain with external flow and mechanical boundaries. A stochastic DFN composed of type I (blue) and type II (green) fractures is embedded in the form of internal discontinuities. An unstructured mesh conforming to the DFN is generated and hybrid elements are highlighted. The meshing code is adapted from the open-source code DistMesh (Persson & Strang, 2004).

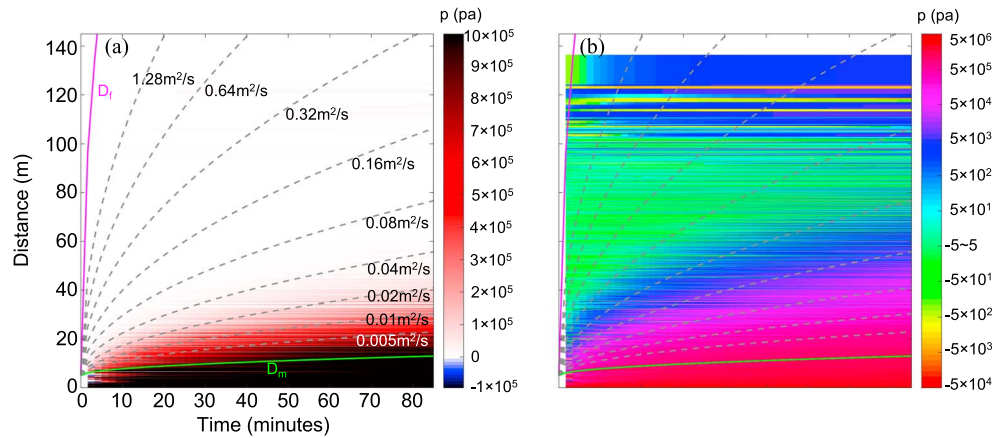
### 6.2. Fluid Pressure

Figure 9, known as the *R-T* plot, shows the modeled spatial-temporal distribution of the fluid pressure. *R* refers to the distance from the domain center (0,0), which is shown on the vertical axis, and *T* refers to the time, which is shown on the horizontal axis. The color indicates the fluid pressure, plotted on both a linear scale (Figure 9a) and a logarithmic scale (Figure 9b). Specific to the latter, it is the quantity  $\log_{10}|p'/5| \times \text{sign}(p')$  that is used for coloring, where  $p'$  is identical to the fluid pressure  $p$  except that any value that is 6 orders of magnitude below the injection pressure  $p_g$  (i.e.,  $-5 \text{ Pa} \sim 5 \text{ Pa}$ ) is rounded to  $-5 \text{ Pa}$  or  $5 \text{ Pa}$ . Overlying both plots are several diffusion fronts, calculated as  $r_i = \sqrt{4\pi D_i t} + 5m$ . Here  $\sqrt{4\pi D_i t}$  defines a characteristic pressure front resulting from a point-source injection of fluid into an isotropic, homogeneous porous medium with a hydraulic diffusivity  $D = k/(\eta C \phi)$  (Shapiro et al., 1997). The upper profile, calculated using  $k_{fi}, C_{fi}$  in Table 2 and  $\phi_f = 1$  (equation (9)), corresponds to the fracture diffusivity  $D_f$ ; the lower profile, calculated using  $\phi_m = 0.25$ ,  $k_{mx} = k_{my} = 1 \text{ mD}$ , and  $C_m$  in Table 2, corresponds to the mean matrix diffusivity  $D_m$ . In Figure 9a, we observe that the delineated pressure front is well constrained between the two profiles; it approximately coincides with the one calculated using a diffusivity of  $0.08 \text{ m}^2/\text{s}$ , which can be regarded as the overall “effective” diffusivity of the

DFN-matrix system. Figure 9b reveals more details of pressure changes that are orders of magnitude lower than the injection pressure. First, within the delineated diffusion front, the DFN leads to a heterogeneous distribution of the pressure magnitude in the *R-T* space, as are shown by the isochromatic “stripes” extending in the horizontal direction; this contrasts with a smooth variation that otherwise occurs in the absence of fractures (e.g., Segall & Lu, 2015). Second, even beyond the delineated diffusion front, noticeable changes in the fluid pressure still occur. These changes are directly attributed to the solid-to-fluid coupling effect that drives changes in the porosity and therefore in the fluid pressure. It is worth noting that such changes cannot be predicted in a pure fluid diffusion process where the solid-to-fluid coupling is absent. In addition, because of the presence of the DFN, these changes are heterogeneous. Depending on the location and the time, the pressure either increases or decreases, suggesting compressive and extensional poroelastic strain and stress, respectively. Furthermore, the solid-to-fluid coupling effect also manifests itself through the fluid

**Table 2**  
Model Nominal Parameters

Parameter		Value
$\eta$	Fluid viscosity	$10^{-3} \text{ Pa}\cdot\text{s}$
$\phi_{m0}$	Matrix initial porosity	0.24–0.26, random
$k_{mx}, k_{my}$	Matrix permeability	0.9–1.1 mD, random
$C_m$	Matrix compressibility	$1.5 \times 10^{-9} \text{ Pa}^{-1}$
$k_{fi}$	Fracture tangential permeability	1000D ( $b \approx 0.11 \text{ mm}$ from equation (19)), $i = 1-100$
$C_{fi}$	Fracture compressibility	$1.5 \times 10^{-7} \text{ Pa}^{-1}$ , $i = 1-100$
$C_\rho$	Fluid compressibility	$5.1 \times 10^{-10} \text{ Pa}^{-1}$
$p_g$	Dirichlet boundary value (fluid pressure)	5 MPa (above an arbitrary initial pore pressure)
$v_h$	Neumann boundary value (flow velocity)	0
$s$	External fluid source	0
$dt$	Time increment for the fluid problem	100 s
$\alpha$	Biot-Willis coefficient	0.8
$E_m$	Matrix Young’s modulus	40 GPa
$\nu_m$	Matrix Poisson’s ratio	0.25
$G_{fi}$	Fracture shear modulus	1 GPa, $i = 1-100$
$\underline{u}_g$	Dirichlet boundary value (displacement)	0
$\underline{t}_h$	Neumann boundary value (traction)	0



**Figure 9.** Modeled spatial-temporal distribution of the fluid pressure. (a) Linear color scale and (b) logarithmic color scale. The maximum pressure is 5 MPa. However, notice in Figure 9a that the color is fully saturated at 1 MPa for better visualization. Two characteristic diffusion profiles derived from the diffusivity of fractures and the matrix are shown respectively as the upper and lower bounds, together with several other in-between profiles. A diffusion front is well delineated in Figure 9a, reflecting the overall “effective” diffusivity of the medium. Figure 9b reveals more details on the effect of the DFN and the solid-to-fluid coupling effect, as are elaborated in the text.

pressure boundary effect, as are shown by the alternating positive and negative pressure changes near the boundary (distance above 100 m) in both Figures 9a and 9b.

Figure 10 shows examples of the spatial distribution of the fluid pressure at four time steps. In Figures 10a–10d, the pressure is plotted on a linear scale. Due to their high conductivity, the injection pressure diffuses primarily along the fractures interconnected back to the boundary of injection (i.e., type II fractures). Diffusion into the matrix is secondary. Overall, the colored area delineates a diffusion-dominated region. In detail, Figures 10e–10h show the pressure on a logarithmic color scale. The DFN causes strong heterogeneity in

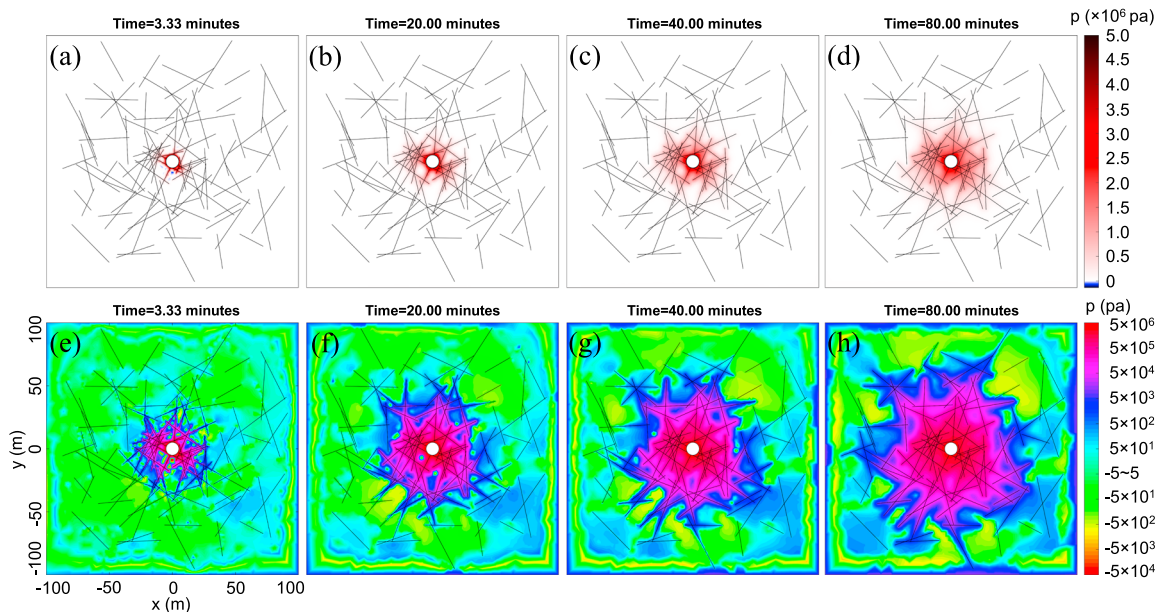


**Figure 10.** Snapshots of the spatial distribution of the fluid pressure at four selected time steps. The time is indicated at the top of each plot. (a–d) Linear color scale and (e–h) logarithmic color scale. The pressure field is continuous but highly heterogeneous due to the DFN. Figures 10a–10d show the major area where the pressure diffusion occurs. Figures 10e–10h further highlight the diffusion-dominated area, as well as the remaining area where the pressure either increases or decreases due to the DFN and the solid-to-fluid coupling effect. Notice also the pressure boundary effect near the edges of the domain as a direct result of the solid-to-fluid coupling effect.

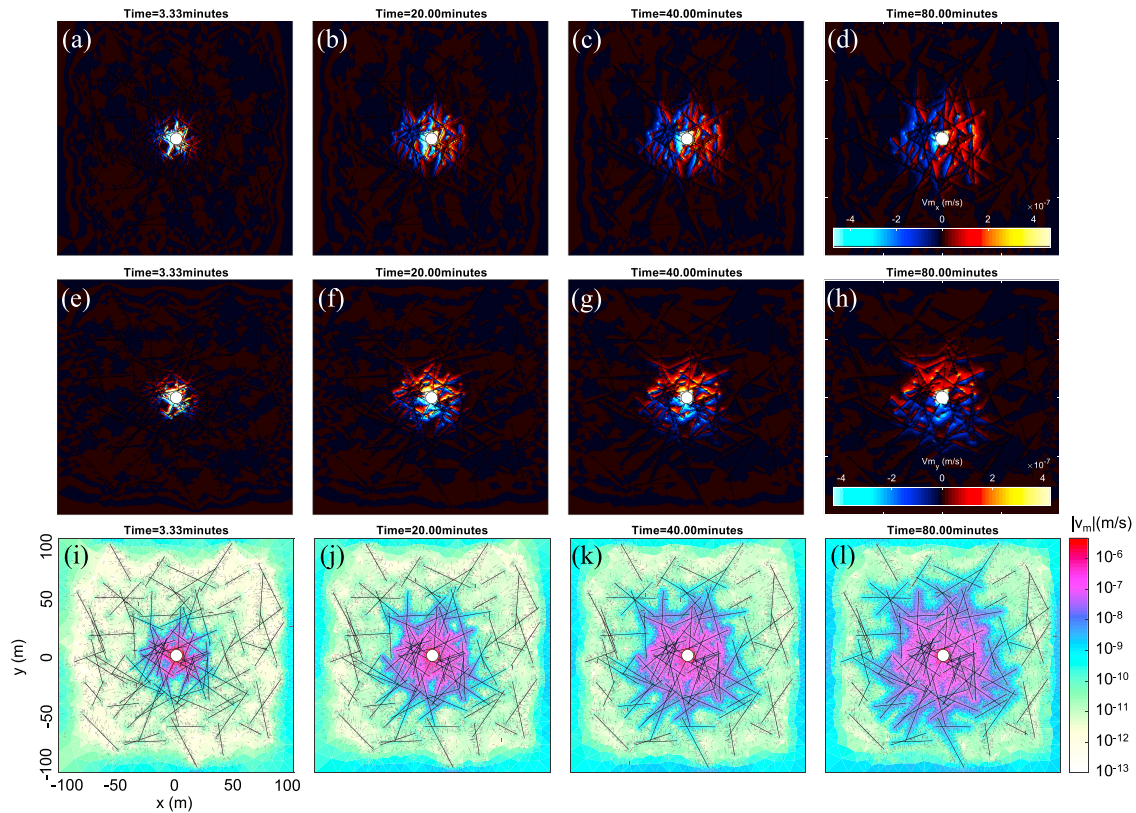


**Figure 11.** Snapshots of the spatial distribution of the flow velocity in the matrix,  $|v_m|$ , at four selected time steps. The time is indicated at the top of each plot. (a–d) The x component on a linear color scale, (e–h) y component on a linear color scale, and (i–l) magnitude on a logarithmic color scale. Both x and y components follow a discontinuous distribution. Notice in Figures 11i–11l, the magnitude of the velocity is on the order of  $10^{-13}$ – $10^{-6}$  m/s. However, in Figures 11a–11h, the color is saturated within the range from  $-4 \times 10^{-7}$  to  $4 \times 10^{-7}$  m/s for better visualization. The distribution of the equivalent body force is expected to be the same after appropriate linear scaling.

the pressure field. Similar to what is observed in Figure 9b, here, outside the diffusion-dominated area and depending on the time and the location relative to fractures, the pressure either increases or decreases, suggesting compressive and extensional poroelastic strain and stress. More details are elaborated following Figure 13.

### 6.3. Flow Velocity (Equivalent Body Force)

Figure 11 shows examples of the spatial distribution of the flow velocity in the matrix,  $v_m$ , calculated at the same selected time steps according to equation (16). The flow velocity within each fracture,  $v_{fj\pi}$ , which is orders of magnitude higher, is not shown. Both x and y components are shown. In addition, a logarithmic quantity,  $\log_{10}|v_m|$ , is also plotted to show the magnitude. The vectors show the directions of  $v_m$  at different locations. It can be seen that the highly conductive fractures act as preferred flow paths, leading to high flow velocities around them. Meanwhile, they behave as hydraulic weak discontinuities, providing fluid to the surrounding matrix and causing  $v_m$  to vary discontinuously across them. We point out that the flow velocity and the equivalent body force are linearly indicative of each other, as is suggested by equations (16) and (25). Therefore, with appropriate scaling, one can expect the equivalent body force to follow the same distribution shown in Figure 11.

### 6.4. Poroelastic Displacement

Figure 12 shows examples of the spatial distribution of the poroelastic displacement at the same selected time steps. Here we observe the following. First, the solid undergoes expansion, leading to overall outward displacements throughout the domain. This arises directly from the fluid-to-solid coupling effect that drives deformation via the (negative) pressure gradient. Second, because of the inclusion of the transverse simple

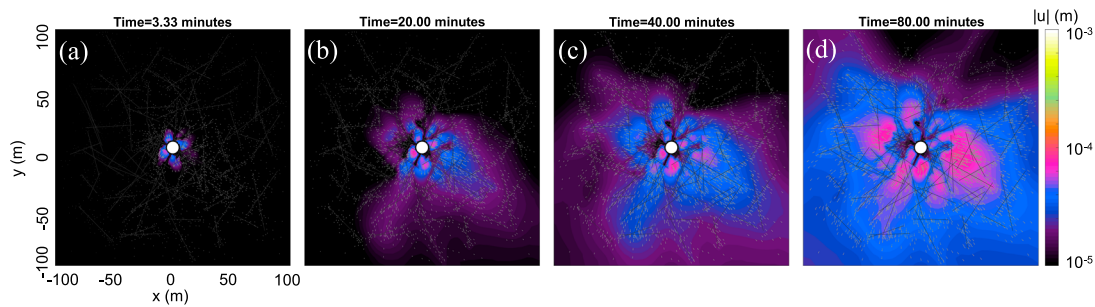


**Figure 12.** Snapshots of the spatial distribution of the poroelastic displacement at four selected time steps. The time is indicated at the top of each plot. The color indicates the logarithmic-scale magnitude, and the vectors indicate the direction. The displacement is outward but nonradial.

shear behavior of fractures in the model, the displacements appear highly dependent on the DFN and are more prominent in some areas than in others. Therefore, notice that the expansion is nonradial and localized. Furthermore, the displacements are continuous but not necessarily smooth across a fracture, as are indicated by the “kinks” in the contours across some fractures.

### 6.5. Poroelastic Stress

Figure 13 shows examples of the spatial distribution of the poroelastic stress (effective, as opposed to total) in the matrix,  $\sigma'_m$ , calculated at the same selected time steps according to equation (27). The stress within fractures is not shown. Note that the domain is subjected to zero traction at the outer periphery and is fixed on the well boundary. The normal components along both  $x$  direction (see Figures 13a–13d) and  $y$  direction (see Figures 13e–13h), as well as the shear component (see Figures 13i–13l), are shown. Here we emphasize that the occurrence of shear stress can only be predicted by including the fluid-to-solid coupling effect (i.e., the poroelastic process). In addition, two quantities,  $I_1'/3$  (see Figures 13m–13p) and  $\sqrt{J_2'}$  (see Figures 13q–13t), are also shown to reflect the mean normal stress and the amount of the shear stress. Here  $I_1'$  and  $J_2'$  are the first stress invariant and the second deviatoric stress invariant, respectively, both calculated from a 3-D effective stress tensor that is obtained by supplementing  $\sigma'_m$  with the remaining five components given by the plane strain solution.

From Figures 13a–13d and Figures 13e–13h, we observe the following regarding the poroelastic normal stress. First, along either  $x$  or  $y$ , due to poroelastic expansion of the solid, overall, the area near the injection undergoes extension, whereas the area further away from the injection undergoes compression, in that direction. Over time, the extensional stress progresses always from the injection to cover more area while the compressive stress recedes toward the outer boundary to cover less area. Second, because of the transverse simple shear behavior of fractures, the distribution of the normal stress appears rather “patchy” and DFN-dependent. This is also reflected in the nonradial expansion of the solid shown in Figure 12. Nonetheless, notice that the normal stress is always continuous in space. Third, the area immediately near a fracture located within the diffusion-dominated region (see Figures 10a–10d) undergoes extensional stress. In other words, if the pressure change within a fracture is predominantly caused by the fluid diffusion rather than the solid-to-fluid coupling, then this fracture tends to expand outward, leading to extensional normal stress immediately near it. This is especially evident in the mean normal stress, see Figures 13m–13p. However, further away from the fracture, compression is possible, and therefore, lastly, we observe compartmentalized compressive stress in areas surrounded by fractures, even though these areas are located within an overall extensional environment.

There is also an excellent agreement between the fluid pressure and the mean poroelastic normal stress. Comparing Figures 10e–10h against Figures 13m–13p, we observe that outside the diffusion-dominated region where the fluid pressure is driven by the solid-to-fluid coupling, compressive mean normal stress coincides with pressure increase, and extensional mean normal stress coincides with pressure decrease, due to porosity reduction and growth, respectively.

The distribution of the poroelastic shear stress turns out more intriguing. It is shown by Figures 13i–13l that in this particular example, overall, quadrants I and III experience positive shear stress (left-lateral sense of shear),



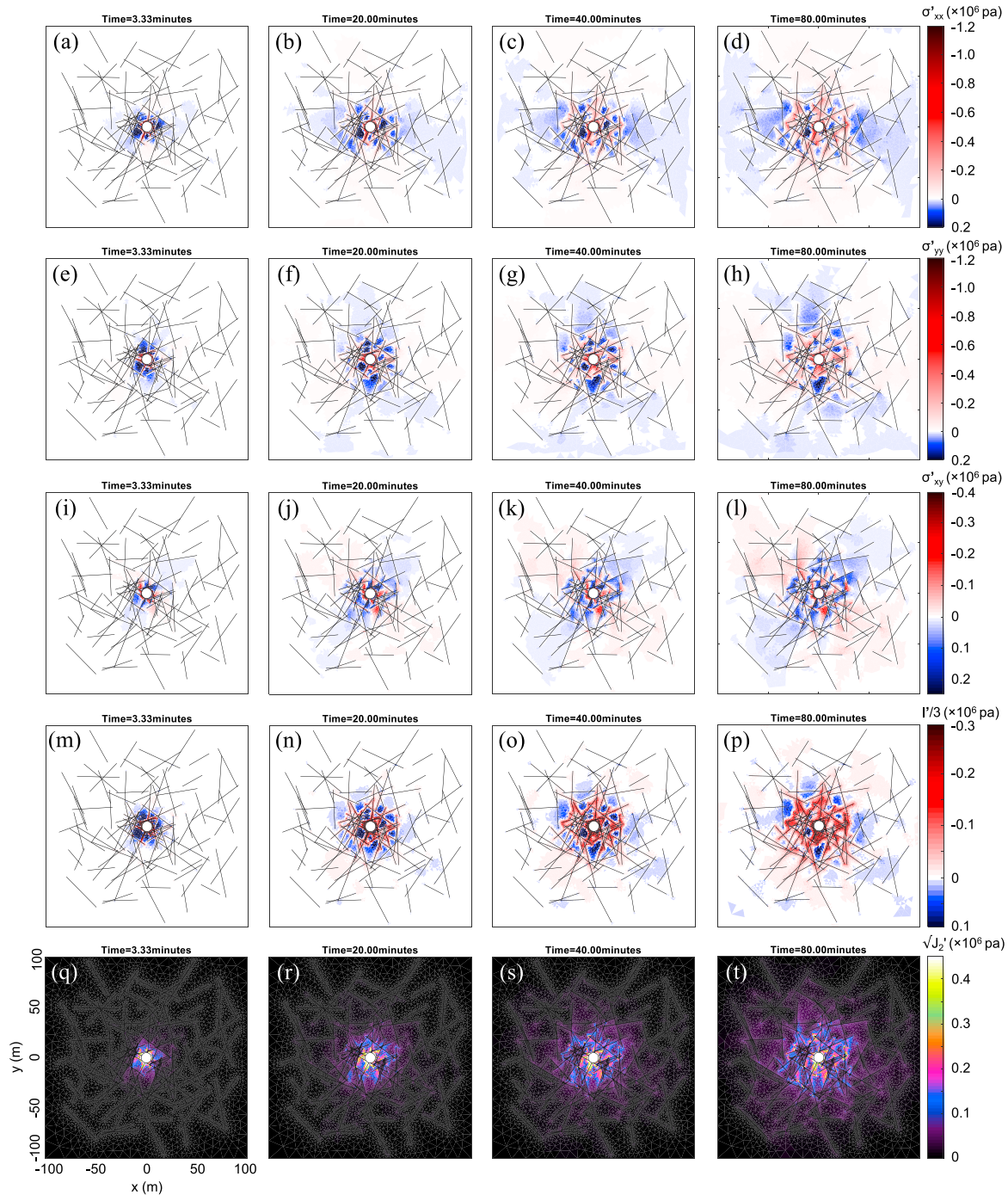


**Figure 13.** Snapshots of the spatial distribution of the effective poroelastic stress tensor in the matrix,  $\sigma'_m$ , at four selected time steps. The time is indicated at the top of each plot. (a–d) The x normal component, (e–h) y normal component, (i–l) shear component, (m–p) mean normal stress, and (q–t) deviatoric stress. Figures 13m–13t are derived based on a plane strain solution. The color is on a linear scale in all plots and is saturated in a range within the modeled maximum and minimum values for better visualization. In Figures 13a–13d, 13e–13h, and 13m–13p, cool color indicates compressive stress whereas warm color indicates extensional stress. Notice that the poroelastic effective stress tensor is markedly different in both spatial distribution and magnitude than that predicted by the fluid-to-solid decoupled approach,  $\sigma'_m(\underline{x}, t) \neq -\alpha p(\underline{x}, t)1$ , where  $p(\underline{x}, t)$  is shown in Figure 10. Notice also the stress heterogeneity, as shown by the patchy distribution, due to the transverse simple shear behavior of fractures.

while quadrants II and IV experience negative shear stress (right-lateral sense of shear). Similar to what is observed for the normal stress, here, in either case, shear in the opposite sense can occur and be compartmentalized. Interestingly, the shear stress can also appear “discontinuous.” This is especially evident in the deviatoric stress, see Figures 13q–13t. It is worth noting that such discontinuities are *apparent discontinuities* as opposed to *true discontinuities*, because the details within lower dimensional fractures are not shown in the asymptotic domain. The shear stress is in fact continuous, but sharp variations can occur within the finite thickness of a fracture, as illustrated in Figure 5. A similar outcome was presented by Chang and Segall (2016) through a simpler configuration in which a single fault with an explicit thickness was discretized as equal-dimensional elements in Comsol. Note that such apparent discontinuities are made possible by two necessary conditions: (1) inclusion of the transverse simple shear behavior, specifically, the second term in equation (74) and (2) nonsymmetrical poroelastic response on the two sides of a fracture.

## 7. Summary and Conclusion

In this study, we established a fully coupled model of transient fluid flow and prefailure quasi-static poroelasticity in a porous medium embedded with an arbitrary network of discrete fractures. The model domain consists of (1) compressible pores and fractures fully saturated with a compressible fluid and (2) a deformable solid with mechanical layering across the fracture zone. The coupled conservation laws were derived within the classic framework of Biot’s theory of poroelasticity but require a twofold reformulation to account for fractures. First, the storage property of the system was redefined by treating fractures as localized “porosity.” Second, in a local reference frame, a separate set of fluid and solid constitutive laws for each individual fracture were included, augmenting the conductivity and stiffness properties of the system. In addition, the fluid within each fracture behaves in a nonlinear fashion, resulting in an overall nonlinear coupled system. Fractures were explicitly represented throughout the formulation, and no upscaling was used.

We then presented in detail the discretization schemes for the model and the computational procedures. Specifically, for the space discretization, we proposed a hybrid-dimensional, equal-low-order, two-field mixed finite element method. Central to the hybrid-dimensionality is that transversal variations in the tangential fluid flux and the shear strain within each fracture are not resolved, as the hydraulic aperture of the fracture and the thickness of the fracture zone are orders of magnitude lower than typical mesh size in the rest of the domain. Instead, a transversal uniformity assumption allows a much more efficient discretization. In the end, fractures introduce no separate nodes, and therefore, no additional degrees of freedom. For the drained poroelastic system, the equal-low-order mixed interpolation scheme suffices as it does not violate the inf-sup stability constraint; therefore, no spurious oscillation in the fluid pressure field is present. For the time discretization, we utilized a fully coupled fully implicit scheme. Within each time step, we employed a fully implicit Newton-Raphson scheme for solving the nonlinear equations. One important outcome of the study is the fracture-related expressions in the fully discrete form of the coupled equations. We showed that fractures translate to the modification and augmentation to the capacity, conductivity, and stiffness matrices, whereas the coupling matrices remain unchanged.

In addition to its general ability to model a more complex poroelastic system, our computational model also offers several advantages. First, the complications due to domain separation, interaction, and regularization that are typically encountered in a DPDP-based approach are avoided. The mass exchange between the matrix and a fracture, depending on the type of the fracture, can be resolved by either admitting discontinuity in the fluid normal flux across it or enforcing local mass conservation as an interface condition. Second, the arbitrary distribution of the DFN is preserved, allowing us to capture the control of a given DFN on the distribution of the fluid pressure and the solid deformation and stress. Therefore, our model can provide more accurate inputs for the study of poromechanical problems like induced seismicity where an explicit representation of a fracture is crucial. Third, the hybrid-dimensional approach provides an efficient numerical solution and allows a relatively large number of fractures to be included. Lastly, the fracture-related modules can be readily turned on and off in the model, allowing us to investigate the sensitivity of the system response to fractures, including their distribution, hydraulic and mechanical properties, and fracture-induced nonlinearity.

The numerical example also offers several insights. First, the distribution of the fluid pressure is characterized by a diffusion-dominated area and a solid-to-fluid-coupling-dominated area, both strongly depending on the

DFN. In both areas, because of the presence of the DFN, the fluid pressure is highly heterogeneous compared to that in a fracture-free system. Nonetheless, an “effective” hydraulic diffusivity can be determined for the fractured system. Within the diffusion-dominated area, the pressure increases primarily along the fractures and secondarily in the matrix, whereas in the coupling-dominated area, the pressure either increases or decreases coinciding with compressive and extensional poroelastic normal stress, respectively. Second, the poroelastic stress is significantly different than that predicted by the fluid-to-solid decoupled approach. In general, within the diffusion-dominated area, extensional poroelastic normal stress occurs, but is of lower magnitude with coupling; outside the diffusion dominated area, compressive poroelastic normal stress occurs; additional shear stress also develops over the entire domain. The latter two cannot be predicted by the decoupled model. Lastly and more interestingly, while the poroelastic normal stress is predominantly extensional immediately near fractures in the diffusion-dominated area, due to fractures acting as finite-thickness deformation zones, the poroelastic stress is highly heterogeneous. Extensional poroelastic stress can be compartmentalized in an overall compressive area, and vice versa. The same happens to shear stress of opposite sense. In addition, the shear stress can vary sharply across fractures, resulting in an apparent loss of the deviatoric stress.

### Notation and Nomenclature

Light-face letters denote scalars; capped and underlined letters, e.g.,  $\hat{a}$  and  $\underline{a}$ , indicate vectors without and with directional dependence; and bold-face letters designate matrices or tensors.  $(\cdot)^T$  is the transpose operator; “ $\cdot$ ” indicates vector dot product, “ $\cdot\cdot$ ” represents double tensor contraction, and  $[\![\cdot]\!] = (\cdot)|_{\Gamma^+} - (\cdot)|_{\Gamma^-}$  defines a jump of a quantity across an interface  $\Gamma$ . In addition, quantities associated with the porous matrix and fractures are labeled using subscript “ $m$ ” and “ $f$ ,” respectively. In particular, subscript  $f_i$  refers to the  $i$ th fracture, with no summation intended over the repeated “ $i$ .” Wherever needed, summation is specified using  $\sum_i$ . Subscript “0” implies initial values. The  $\partial_t$  and  $(\cdot)$  indicates local and total time derivatives, respectively, and  $\partial(\cdot)$  is used exclusively to indicate domain boundaries. Moreover, a default global Cartesian system  $\underline{x} = (x, y)$  and a set of local coordinate systems  $\underline{\xi}_{f_i} = (\tau_{f_i}, n_{f_i})$  are used, where, “ $\tau_{f_i}$ ” and “ $n_{f_i}$ ” represent the local fracture tangential and normal directions, respectively. The  $\nabla$  and  $\nabla\cdot$  are the gradient operator and divergence operator in  $\underline{x}$ , whereas  $\nabla_\tau$  and  $\nabla_n$  are the local tangential and normal gradient operators in  $\underline{\xi}_{f_i}$ . Note that “ $f_i$ ” is not specifically labeled for these two operators; however, when used, they imply local fracture directions. Further note that subscript “ $f_i\tau$ ” implies that the  $i$ th fracture-related quantity is defined only along the tangential direction (or has only a tangential component), whereas subscript “ $f_i$ ” indicates the projection of a quantity along the tangential direction.

Domain and boundary	
$\Omega, \Omega^{asy}$	computational domain, asymptotic domain
$\partial\Omega$	domain boundary
$\partial\Omega_p, \partial\Omega_v$	fluid Dirichlet boundary, fluid Neumann boundary
$\partial\Omega_u, \partial\Omega_\tau$	solid Dirichlet boundary, solid Neumann boundary
$\partial f, \partial f^I, \partial f^{II}$	fracture surface, type I fracture, type II fracture
$b_H, b_M$	fracture hydraulic aperture, fracture zone thickness, m
$\theta$	fracture orientation, deg
$l$	fracture length, m
$n_f, n_{fI}, n_{fII}$	number of fractures, type I fractures and type II fractures
Fluid	
$\phi, \Phi$	intrinsic porosity, partial porosity, [–]
$V, V^\phi$	total volume, pore volume, m <sup>3</sup>
$\Lambda$	geometry parameter, [–]
$C$	compressibility, Pa <sup>–1</sup>
$\eta$	fluid viscosity, Pa·s
$\kappa, \kappa$	conductivity tensor, fracture tangential conductivity, m <sup>2</sup> /(Pa·s)
$\mathbf{k}, k$	permeability tensor, fracture tangential permeability, m <sup>2</sup>
$\rho$	fluid density, kg/m <sup>3</sup>
$\underline{v}, v_h$	flow velocity, fluid Neumann boundary value, m <sup>2</sup> /s
$S$	external fluid source/sink, kg/(m <sup>3</sup> s)

$s$	external fluid source/sink divided by the initial fluid density, $s^{-1}$
$p, p_g$	fluid pressure (relative to an initial state), fluid Dirichlet boundary value, Pa
<b>Solid</b>	
$\mathbf{D}$	elastic stiffness tensor, Pa
$E, G$	Young's modulus, fracture shear modulus, Pa
$\nu$	Poisson's ratio, [–]
$\underline{u}, \underline{u}_g$	displacement (relative to an initial state), solid Dirichlet boundary value, m
$\underline{t}, \underline{t}_h$	traction, solid Neumann boundary value, Pa
$\underline{\epsilon}$	strain tensor, [–]
$\gamma$	fracture simple shear strain, [–]
$\underline{\sigma}', \underline{\sigma}$	effective stress tensor, Cauchy total stress tensor, Pa
$\sigma_{nr}$	fracture shear stress, Pa
$\mathbf{1}, \underline{1}$	unit identity tensor (Kronecker delta), unit identity vector in Voigt notation, [–]
$\underline{f}_b, \underline{f}_p$	body force, equivalent body force due to pressure gradient, $N/m^3$
<b>Coupling</b>	
$\alpha$	Biot-Willis coefficient, [–]
<b>Weak formulation, discretization, and iteration</b>	
$w$	virtual pressure
$\underline{\eta}$	virtual displacement
$\mathbf{Q}, \mathbf{L}$	dimensional transformation matrices
$\mathbf{R}$	rotation matrix
$\hat{\zeta}, \hat{c}$	nodal fluid pressure, nodal virtual pressure
$\underline{d}, \underline{d}_p$	nodal solid displacement, nodal virtual displacement
$\underline{\zeta}$	combined primary unknown vector, $(\hat{\zeta}, \underline{d})$
$\mathbf{N}, \mathbf{N}$	shape functions for the fluid problem and the solid problem
$\mathbf{B}$	displacement-strain transformation matrix
$\underline{b}$	displacement-volumetric strain transformation vector
$\mathbf{M}$	capacity matrix
$\mathbf{K}$	conductivity matrix
$\mathbf{G}$	stiffness matrix
$\mathbf{C}$	coupling matrix
$\underline{F}$	external nodal mass
$\underline{Y}$	external nodal force
$\mathbf{J}$	Jacobian matrix
$\underline{R}$	residual vector
$dt$	time increment, s
$H$	superscript indicating a hybrid domain or element
$(n), (n + 1)$	subscripts indicating current and next time steps
$(k), (k + 1)$	subscripts indicating current and next iteration steps

## Appendix A

### A.1 The Dual-Porosity Double-Permeability (DPDP) Fluid Model

In the DPDP fluid model, the domain is partitioned into a porous matrix domain and a fracture domain. Both domains are fully saturated with a single-phase fluid that follows a linear Darcy's law and are governed by their respective conservation laws, which interact via a common mass exchange term (Barenblatt et al., 1960; Warren & Root, 1963):

$$\begin{aligned} \nabla \cdot (\rho \eta^{-1} \mathbf{k}_m \cdot \nabla p_m) &= \frac{\partial}{\partial t} (\rho \phi_m) + \Gamma (p_m - p_f) + S_m \text{ on } \Omega_m \\ \nabla \cdot (\rho \eta^{-1} \mathbf{k}_f \cdot \nabla p_f) &= \frac{\partial}{\partial t} (\rho \phi_f) - \Gamma (p_m - p_f) + S_f \text{ on } \Omega_f \end{aligned} \quad (\text{A1})$$

where  $\rho$  is the fluid density;  $\eta$  is the fluid viscosity;  $\mathbf{k}$  is the permeability tensor;  $\phi$  is the intrinsic porosity;  $p$  is the fluid pressure;  $S$  is the external fluid source/sink term; and  $\Gamma$  is the shape factor, the calculation of which requires upscaling; and subscripts  $m$  and  $f$  denote the matrix domain and the fracture domain, respectively. Typically,  $\phi_f = 1$ .

**Table A1**
*Pseudocode for Asymptotic Model Domain Setup and Hybrid Element Identification*

```

1. Generate (or import) a 2-D asymptotic model domain with a pre-defined DFN containing  $n_f$  1-D fractures
2. Store  $\theta(i)$ ; determine  $l_i(x) = a(i)*x - y + c(i)$ ,  $i = 1 \sim n_f$ ; Store index of type I and type II fractures as  $F^I$  and  $F^{II}$ 
3. Conforming meshing into linear triangular elements; calculate element area  $A(i)$ 
4. Set up a node identification mismatch function Findnode with a pre-defined tolerance
5. Set up a function Findelement for identifying elements containing a certain type of nodes
6. Using Findnode and Findelement
  6.1 Identify boundary nodes and boundary elements
  6.2 Identify fracture nodes and hybrid elements
      for  $k = 1: n_f$ 
          Identify the fracture node index (FNI) vector of the  $k$ th fracture (FNIK);  $FNI = [FNI; FNIK]$ 
          Identify the hybrid element index (HEI) vector of the  $k$ th fracture (HEIk);  $HEI = [HEI; HEIk]$ 
          Store a vector indicating the type of fracture these hybrid elements are associated with (HEFT)
          if  $k \in F^I$ , HEFTk = ones(length(HEIk),1)*1;
          elseif  $k \in F^{II}$ , HEFTk = ones(length(HEIk),1)*2;
          end
          HEFT = [HEFT; HEFTk];
          Identify the index of the fracture a hybrid element is associated with (HEFI)
          HEFI = [HEFI; ones(length(HEIk),1)*k]
      end
7. Determine the positivity/negativity of a hybrid element with respect to a conforming fracture
  for  $i = 1: \text{length}(HEI)$ 
       $\bar{x} = \text{mean}(x(i))$ ;  $\text{indicator}(i) = l_i(\bar{x})$ 
      if  $\text{indicator}(i) > 0$ ,  $\underline{n}(i) = [\sin(\theta(HEFI(i))); -\cos(\theta(HEFI(i)))]$ 
      else  $\underline{n}(i) = [-\sin(\theta(HEFI(i))); \cos(\theta(HEFI(i)))]$ 
      end
  end
end
    
```

## A.2 The Solid-to-Fluid Coupling Term

Denote the bulk modulus of the bulk volume, the solid skeleton, and the fluid-filled pore as  $K$ ,  $K_s$ , and  $K_\Phi$ . Here the pore broadly refers to both the matrix pore and fractures. Correspondingly, the volumetric changes resulted from an unit amount of mean stress/isotropic confining pressure are then  $1/K$ ,  $1/K_s$ , and  $1/K_\Phi$ , which satisfy the following relationship:

$$\frac{1}{K} = \frac{1}{K_s} + \frac{1}{K_\Phi} \quad (\text{A2})$$

Denote the total volumetric strain as  $\epsilon_v$  ( $\epsilon_v = \nabla \cdot \underline{u}$ ), and the change in the porosity, either intrinsic or partial, as  $\delta\Phi$ . The ratio between the two quantities thus follows

$$\frac{\delta\Phi}{\nabla \cdot \underline{u}} = \frac{\delta V_\Phi / V_0}{\delta V / V_0} = \frac{1/K_\Phi}{1/K} = \frac{1/K - 1/K_s}{1/K} = 1 - \frac{K}{K_s} = \alpha \quad (\text{A3})$$

where  $\delta V_\Phi$  and  $\delta V$  indicate changes in the pore volume and the total volume, respectively, and  $V_0$  indicates the initial total volume.

Therefore,  $\alpha \nabla \cdot \underline{u}(\underline{x}, t)$  quantifies the change in the porosity.

**Table A2**
*Pseudocode for Computing Element-Wise  $\Lambda_0(\underline{x})$* 

```

1. Assign (or import) the hydraulic properties of matrix and fractures
2. Back calculate  $b_H(i)$  ( $i = 1 \sim n_f$ ) from equation (19) using given fracture permeability
3. Set up a function FNN to determine the local fracture node number in a hybrid element (shown in Table 1)
4.  $\Lambda_0 = \text{ones}(ne, 1)$ ; % ne = total number of elements
  for  $i = 1: \text{length}(HEI)$ 
      Using FNN, determine the local fracture node number  $lfn(1)$  and  $lfn(2)$ 
      Using  $lfn(1)$  and  $lfn(2)$ , calculate fracture line element length  $le$ 
       $\Lambda_0(HEI(i)) = 1/(1/\Lambda_0(HEI(i)) + (0.5*b_H(HEFI(i))*le)/A(HEI(i)))$ 
  end
end
    
```

**Table A3**
*Pseudocode for Augmenting the Elemental Matrices due to Fractures Within the Jacobian and Residual*

1. Compute elemental  $\mathbf{M}^{me}$ ,  $\mathbf{K}^{me}$ , and  $\mathbf{G}^{me}$  of the fracture-free discrete system (the first terms in equations (72), (73), and (74))
  2. Execute elemental modifications to the initial Jacobian and residual
    - for  $i = 1: \text{length}(HEI)$ 
      - 2.1 Determine  $lfn(1)$ ,  $lfn(2)$ ,  $le$  (see Table A2); compute  $N_{\bar{n}}$
      - 2.2 Determine  $\mathbf{Q}_{\bar{n}}$  and  $\mathbf{L}_{\bar{n}}$  in Table 1 from  $lfn(1) + lfn(2) = 3, 4$  or  $5$
      - 2.3 Compute  $\mathbf{M}^{fe}(i)$ ,  $\mathbf{K}^{fe}(i)$  due to fractures using  $b_{Hj0}$  (the second terms in equations (72) and (73))
      - 2.4 Compute  $\mathbf{G}^{fe}(i)$  using  $b_{Mi}$  (the second term in equation (74))
      - 2.5 Compute  $\mathbf{K}^{tre}$  due to mass transfer
        - 2.5.1 if HEFT( $i$ ) = 1, compute  $\mathbf{K}^{mfe}$  using  $b_{Hj0}$  (third term in equation (73)),  $\mathbf{K}^{tre}(i) = \mathbf{K}^{mfe}/2$ ; end
        - 2.5.2 if HEFT( $i$ ) = 2, compute the following as part of the fourth term in equation (73):  

$$\mathbf{K}^{fme} = -\{(\mathbf{Q}_{\bar{n}} * N_{\bar{n}} * r(i) * \mathbf{K}_m(HEI(i)) * \text{grad}(N_m(HEI(i)))) d\Gamma; \mathbf{K}^{tre}(i) = \mathbf{K}^{fme}; \text{end}$$
    - 2.6 Elemental modification (halved before global assembly)
      - 2.6.1  $\mathbf{M}^{me}(HEI(i)) = \mathbf{M}^{me}(HEI(i)) + \mathbf{M}^{fe}(i)/2$ ;
      - 2.6.2  $\mathbf{K}^{me}(HEI(i)) = \mathbf{K}^{me}(HEI(i)) + \mathbf{K}^{fe}(i)/2 + \mathbf{K}^{tre}(i)$ ;
      - 2.6.3  $\mathbf{G}^{me}(HEI(i)) = \mathbf{G}^{me}(HEI(i)) + \mathbf{G}^{fe}(i)/2$ ;
  - end
3. Within each Newton-Raphson iteration, update elemental modifications to the Jacobian and residual:
  - for  $i = 1: \text{length}(HEI)$ 
    - 3.1 Get the average fracture nodal pressure:  $\zeta_{\bar{n}} = (\zeta(lfn(1)) + \zeta(lfn(2)))/2$ ;
    - 3.2 Compute coefficient  $a_i$  from  $\zeta_{\bar{n}}$  (equation (84))
    - 3.3 Update  $\mathbf{M}^{fe}(i)$ ,  $\mathbf{K}^{fe}(i)$  from 2.3,  $\mathbf{K}^{mfe}$  from 2.5.1 for the Jacobian (equation (86))
      - 3.3.1  $\mathbf{M}^{fe}(i) = \mathbf{M}^{fe}(i) \times (a_i + C_{\bar{n}} \times \zeta_{\bar{n}})$ ;
      - $\mathbf{K}^{fe}(i) = \mathbf{K}^{fe}(i) \times (a_i^3 + 3a_i^2 \times C_{\bar{n}} \times \zeta_{\bar{n}})$ ;
      - $\mathbf{K}^{mfe} = \mathbf{K}^{mfe} \times (a_i^2 + 2a_i \times C_{\bar{n}} \times \zeta_{\bar{n}})$ ;  $\mathbf{K}^{tre}(i) = \mathbf{K}^{mfe}/2$ ;
    - 3.3.2 Repeat 2.6.1, 2.6.2
  - 3.4 Update  $\mathbf{M}^{fe}(i)$ ,  $\mathbf{K}^{fe}(i)$  from 2.3,  $\mathbf{K}^{mfe}$  from 2.5.1 for the residual (equations (82) and (83))
    - 3.4.1  $\mathbf{M}^{fe}(i) = \mathbf{M}^{fe}(i) \times a_i$
    - $\mathbf{K}^{fe}(i) = \mathbf{K}^{fe}(i) \times a_i^3$
    - $\mathbf{K}^{mfe} = \mathbf{K}^{mfe} \times a_i^2$ ;  $\mathbf{K}^{tre}(i) = \mathbf{K}^{mfe}/2$ ;
  - 3.4.2 Repeat 2.6.1, 2.6.2
- end

### A.3 Discrete Fracture Network Implementation

Here the pseudocode for two steps and one subroutine pertaining to implementing a predefined DFN is given. The other steps, including assigning material properties, generating finite element data processing arrays, computing element-wise matrices and vectors, assembling global matrices and vectors, backward Euler time-stepping, and Newton-Raphson iteration, can be completed following standard procedures; the details of those steps are omitted (Table A1).

Repeated values in  $HEI$  indicate elements conforming to multiple fractures. We are now in a position to revisit the geometry-dependent parameter,  $\Lambda_0(\underline{x})$ . Equation (4) states that  $\Lambda_0(\underline{x})$  can be calculated by splitting the fracture elemental volume in the computational domain into two equal parts and allocating them to the two conforming hybrid elements. For a 2-D problem,  $\Lambda_0(\underline{x})$  reads

$$\Lambda_0(\underline{x}) = \begin{cases} \frac{A^H}{A^H + \frac{1}{2} \sum_r^{ncf} b_r l_r^e}, & \underline{x} \in \Omega^H \\ 1, & \text{elsewhere} \end{cases} \quad (\text{A4})$$

where  $A^H$  is the area of a hybrid element,  $ncf$  is the number of fractures a hybrid element conforms to,  $b_r$  is the thickness of the  $r$ th conforming fracture, and  $l_r^e$  is the length of the line element on the  $r$ th conforming fracture. The pseudocode shown in Table A2 automatically considers multiple fractures conforming to a hybrid element.

Based on sections 4.3 and 5, we include the effect of fractures by implementing the following subroutine (Table A3), which automatically accounted for multiple conforming fractures. Further, the positive and negative hybrid elements with respect to a conforming fracture are separately tackled using their respective  $\underline{n}$  (see Table A1); the full discontinuity term is ensured upon assembly of the global  $\mathbf{K}$ .

#### Acknowledgments

We thank Ronaldo Borja, Paul Segall, Norm Sleep, Timur Garipov, Nicola Castelletto, and Mohammad Karimi-Fard for their discussion. We also thank the two reviewers for their comments and suggestions. Funding to L. Jin is provided by the Stanford Center for Induced and Triggered Seismicity and the Stanford Rock Physics and Borehole Geophysics Project. No data was used in producing this manuscript.

#### References

- Angot, P., Boyer, F., & Hubert, F. (2009). Asymptotic and numerical modelling of flows in fractured porous media. *ESAIM: Mathematical Modelling and Numerical Analysis*, 43(02), 239–275.
- Antonietti, P. F., Formaggia, L., Scotti, A., Verani, M., & Verzotti, N. (2015). Mimetic finite difference approximation of flows in fractured porous media (No. 20, p. 2015). MOX Report.
- Armero, F., & Callari, C. (1999). An analysis of strong discontinuities in a saturated poro-plastic solid. *International Journal for Numerical Methods in Engineering*, 46(10), 1673–1698.
- Aziz, K., & Settari, A. (1979). *Petroleum reservoir simulation*. Calgary: Chapman & Hall.
- Baca, R. G., Arnett, R. C., & Langford, D. W. (1984). Modelling fluid flow in fractured-porous rock masses by finite-element techniques. *International Journal for Numerical Methods in Fluids*, 4(4), 337–348.
- Barenblatt, G. I., Zheltov, I. P., & Kochina, I. Formaggia, N. (1960). Basic concepts in the theory of seepage of homogeneous liquids in fissured rocks [strata]. *Journal of Applied Mathematics and Mechanics*, 24(5), 1286–1303.
- Beavers, G. S., & Joseph, D. D. (1967). Boundary conditions at a naturally permeable wall. *Journal of Fluid Mechanics*, 30(01), 197–207.
- Berkowitz, B. (2002). Characterizing flow and transport in fractured geological media: A review. *Advances in Water Resources*, 25(8), 861–884.
- Berkowitz, B., Bear, J., & Braester, C. (1988). Continuum models for contaminant transport in fractured porous formations. *Water Resources Research*, 24(8), 1225–1236.
- Biot, M. A. (1941). General theory of three-dimensional consolidation. *Journal of Applied Physics*, 12(2), 155–164.
- Booker, J. R., & Carter, J. P. (1986). Analysis of a point sink embedded in a porous elastic half space. *International Journal for Numerical and Analytical Methods in Geomechanics*, 10(2), 137–150.
- Borja, R. I. (2013). *Plasticity*. Berlin: Springer.
- Castelletto, N., Gambolati, G., & Teatini, P. (2015a). A coupled MFE poromechanical model of a large-scale load experiment at the coastland of Venice. *Computational Geosciences*, 19(1), 17.
- Castelletto, N., White, J. A., & Tchelepi, H. A. (2015b). Accuracy and convergence properties of the fixed-stress iterative solution of two-way coupled poromechanics. *International Journal for Numerical and Analytical Methods in Geomechanics*, 39(14), 1593–1618.
- Castelletto, N., Hajibeygi, H., & Tchelepi, H. A. (2017). Multiscale finite-element method for linear elastic geomechanics. *Journal of Computational Physics*, 331, 337–356.
- Cerfontaine, B., Dieudonné, A. C., Radu, J. P., Collin, F., & Charlier, R. (2015). 3D zero-thickness coupled interface finite element: Formulation and application. *Computers and Geotechnics*, 69, 124–140.
- Chang, K. W., & Segall, P. (2016). Injection-induced seismicity on basement faults including poroelastic stressing. *Journal of Geophysical Research - Solid Earth*, 121, 2708–2726. <https://doi.org/10.1002/2015JB012561>
- Chen, T., Clauser, C., Marquart, G., Willbrand, K., & Mottaghy, D. (2015). A new upscaling method for fractured porous media. *Advances in Water Resources*, 80, 60–68.
- Choo, J., & Borja, R. I. (2015). Stabilized mixed finite elements for deformable porous media with double porosity. *Computer Methods in Applied Mechanics and Engineering*, 293, 131–154.
- Cleary, M. P. (1977). Fundamental solutions for a fluid-saturated porous solid. *International Journal of Solids and Structures*, 13(9), 785–806.
- Dereims, A., Drapier, S., Bergheau, J. M., & De Luca, P. (2015). 3D robust iterative coupling of Stokes, Darcy and solid mechanics for low permeability media undergoing finite strains. *Finite Elements in Analysis and Design*, 94, 1–15.
- Dietrich, P., Helmig, R., Sauter, M., Hötzel, H., Köngeter, J., & Teutsch, G. (Eds.) (2005). *Flow and Transport in Fractured Porous Media*. Berlin: Springer Science & Business Media.
- Elsworth, D., & Bai, M. (1992). Flow-deformation response of dual-porosity media. *Journal of Geotechnical Engineering*, 118(1), 107–124.
- Erhel, J., De Dreuzy, J. R., & Poirriez, B. (2009). Flow simulation in three-dimensional discrete fracture networks. *SIAM Journal on Scientific Computing*, 31(4), 2688–2705.
- Faille, I., Fumagalli, A., Jaffré, J., & Roberts, J. E. (2016). Model reduction and discretization using hybrid finite volumes for flow in porous media containing faults. *Computational Geosciences*, 1–23.
- Ferronato, M., Castelletto, N., & Gambolati, G. (2010). A fully coupled 3-D mixed finite element model of Biot consolidation. *Journal of Computational Physics*, 229(12), 4813–4830.
- Formaggia, L., Fumagalli, A., Scotti, A., & Ruffo, P. (2014). A reduced model for Darcy's problem in networks of fractures. *ESAIM. Mathematical Modelling and Numerical Analysis*, 48(4), 1089.
- Garipov, T. T., Karimi-Fard, M., & Tchelepi, H. A. (2016). Discrete fracture model for coupled flow and geomechanics. *Computational Geosciences*, 20, 149–160.
- Gebauer, S., Neunhüserer, L., Kornhuber, R., Ochs, S., Hinkelmann, R., & Helmig, R. (2002). Equidimensional modelling of flow and transport processes in fractured porous systems I. *Developments in Water Science*, 47, 335–342.
- Geiger, S., Roberts, S., Matthäi, S. K., Zoppou, C., & Burri, A. (2004). Combining finite element and finite volume methods for efficient multiphase flow simulations in highly heterogeneous and structurally complex geologic media. *Geofluids*, 4(4), 284–299.
- Gelet, R., Loret, B., & Khalili, N. (2012). A thermo-hydro-mechanical coupled model in local thermal non-equilibrium for fractured HDR reservoir with double porosity. *Journal of Geophysical Research*, 117, B07205. <https://doi.org/10.1029/2012JB009161>
- Hansbo, A., & Hansbo, P. (2004). A finite element method for the simulation of strong and weak discontinuities in solid mechanics. *Computer Methods in Applied Mechanics and Engineering*, 193(33), 3523–3540.
- Hardebol, N. J., Maier, C., Nick, H., Geiger, S., Bertotti, G., & Boro, H. (2015). Multiscale fracture network characterization and impact on flow: A case study on the Latemar carbonate platform. *Journal of Geophysical Research - Solid Earth*, 120, 8197–8222. <https://doi.org/10.1002/2015JB011879>
- Hirthe, E. M., & Graf, T. (2015). Fracture network optimization for simulating 2D variable-density flow and transport. *Advances in Water Resources*, 83, 364–375.

- Hou, T. Y., & Wu, X. H. (1997). A multiscale finite element method for elliptic problems in composite materials and porous media. *Journal of Computational Physics*, *134*(1), 169–189.
- Hu, M., Wang, Y., & Rutqvist, J. (2017). Fully coupled hydro-mechanical numerical manifold modeling of porous rock with dominant fractures. *Acta Geotechnica*, *12*(2), 231–252.
- Hudson, J. A., & Liu, E. (1999). Effective elastic properties of heavily faulted structures. *Geophysics*, *64*(2), 479–485.
- Hughes, T. J. (2012). *The Finite Element Method: Linear Static and Dynamic Finite Element Analysis*. Englewood Cliffs, NJ: Courier Corporation.
- Hyman, J. D., Karra, S., Makedonska, N., Gable, C. W., Painter, S. L., & Viswanathan, H. S. (2015). dfnWorks: A discrete fracture network framework for modeling subsurface flow and transport. *Computational Geosciences*, *84*, 10–19.
- Jha, B., & Juanes, R. (2007). A locally conservative finite element framework for the simulation of coupled flow and reservoir geomechanics. *Acta Geotechnica*, *2*(3), 139–153.
- Juanes, R., Samper, J., & Molinero, J. (2002). A general and efficient formulation of fractures and boundary conditions in the finite element method. *International Journal for Numerical Methods in Engineering*, *54*(12), 1751–1774.
- Karimi-Fard, M., & Firoozabadi, A. (2003). Numerical simulation of water injection in fractured media using the discrete-fracture model and the Galerkin method. *SPE Reservoir Evaluation and Engineering*, *6*(02), 117–126.
- Karimi-Fard, M., Durlofsky, L. J., & Aziz, K. (2003). An efficient discrete fracture model applicable for general purpose reservoir simulators. In SPE Reservoir Simulation Symposium. Society of Petroleum Engineers.
- Khalili, N., & Selvadurai, A. P. S. (2003). A fully coupled constitutive model for thermo-hydro-mechanical analysis in elastic media with double porosity. *Geophysical Research Letters*, *30*(24), 2268. <https://doi.org/10.1029/2003GL018838>
- Kim, J. G., & Deo, M. D. (2000). Finite element, discrete-fracture model for multiphase flow in porous media. *AIChE Journal*, *46*(6), 1120–1130.
- Kim, J., Tchelepi, H. A., & Juanes, R. (2011). Stability and convergence of sequential methods for coupled flow and geomechanics: Fixed-stress and fixed-strain splits. *Computer Methods in Applied Mechanics and Engineering*, *200*(13), 1591–1606.
- Korsawe, J., Starke, G., Wang, W., & Kolditz, O. (2006). Finite element analysis of poro-elastic consolidation in porous media: Standard and mixed approaches. *Computer Methods in Applied Mechanics and Engineering*, *195*(9), 1096–1115.
- Lamb, A. R., Gorman, G. J., & Elsworth, D. (2013). A fracture mapping and extended finite element scheme for coupled deformation and fluid flow in fractured porous media. *International Journal for Numerical and Analytical Methods in Geomechanics*, *37*(17), 2916–2936.
- Lee, S. H., Lough, M. F., & Jensen, C. L. (2001). Hierarchical modeling of flow in naturally fractured formations with multiple length scales. *Water Resources Research*, *37*(3), 443–455.
- Lim, K. T., & Aziz, K. (1995). Matrix-fracture transfer shape factors for dual-porosity simulators. *Journal of Petroleum Science and Engineering*, *13*(3), 169–178.
- Liu, E., Hudson, J. A., & Pointer, T. (2000). Equivalent medium representation of fractured rock. *Journal of Geophysical Research*, *105*(B2), 2981–3000.
- Luege, M., Lucero, J., Torrijos, C., & Orlando, A. (2015). Coupled mechanical and fluid flow analysis in fractured saturated porous media using the XFEM. *Applied Mathematical Modelling*, *40*, 4480–4504.
- Martin, V., Jaffré, J., & Roberts, J. E. (2005). Modeling fractures and barriers as interfaces for flow in porous media. *SIAM Journal on Scientific Computing*, *26*(5), 1667–1691.
- Meschke, G., & Leonhart, D. (2015). A Generalized Finite Element Method for hydro-mechanically coupled analysis of hydraulic fracturing problems using space-time variant enrichment functions. *Computer Methods in Applied Mechanics and Engineering*, *290*, 438–465.
- Mustapha, H. (2014). A Gabriel-Delaunay triangulation of 2D complex fractured media for multiphase flow simulations. *Computational Geosciences*, *18*(6), 989–1008.
- Noetinger, B. (2015). A quasi steady state method for solving transient Darcy flow in complex 3D fractured networks accounting for matrix to fracture flow. *Journal of Computational Physics*, *283*, 205–223.
- Noetinger, B., & Jarrige, N. (2012). A quasi steady state method for solving transient Darcy flow in complex 3D fractured networks. *Journal of Computational Physics*, *231*(1), 23–38.
- Norbeck, J. H., McClure, M. W., Lo, J. W., & Horne, R. N. (2015). An embedded fracture modeling framework for simulation of hydraulic fracturing and shear stimulation. *Computational Geosciences*, *20*, 1–18.
- Nordbotten, J. M. (2014). Finite volume hydromechanical simulation in porous media. *Water Resources Research*, *50*(5), 4379–4394.
- Persson, P. O., & Strang, G. (2004). A simple mesh generator in MATLAB. *SIAM Review*, *46*(2), 329–345.
- Pouya, A. (2012). Three-dimensional flow in fractured porous media: A potential solution based on singular integral equations. *Advances in Water Resources*, *35*, 30–40.
- Pouya, A. (2015). A finite element method for modeling coupled flow and deformation in porous fractured media. *International Journal for Numerical and Analytical Methods in Geomechanics*, *39*(16), 1836–1852.
- Prévost, J. H., & Sukumar, N. (2016). Faults simulations for three-dimensional reservoir-geomechanical models with the extended finite element method. *Journal of the Mechanics and Physics of Solids*, *86*, 1–18.
- Reichenberger, V., Jakobs, H., Bastian, P., & Helmig, R. (2006). A mixed-dimensional finite volume method for two-phase flow in fractured porous media. *Advances in Water Resources*, *29*(7), 1020–1036.
- Rohmer, J., Nguyen, T. K., & Torabi, A. (2015). Off-fault shear failure potential enhanced by high-stiff/low-permeable damage zone during fluid injection in porous reservoirs. *Geophysical Journal International*, *202*(3), 1566–1580.
- Rudnicki, J. W. (1986). Fluid mass sources and point forces in linear elastic diffusive solids. *Mechanics of Materials*, *5*(4), 383–393.
- Rutqvist, J., & Stephansson, O. (2003). The role of hydromechanical coupling in fractured rock engineering. *Hydrogeology Journal*, *11*(1), 7–40.
- Salimzadeh, S., & Khalili, N. (2015). Three-dimensional numerical model for double-porosity media with two miscible fluids including geomechanical response. *International Journal of Geomechanics*, *16*(3), 04015065
- Sandve, T. H., Berre, I., & Nordbotten, J. M. (2012). An efficient multi-point flux approximation method for Discrete Fracture–Matrix simulations. *Journal of Computational Physics*, *231*(9), 3784–3800.
- Sandve, T. H., Keilegavlen, E., & Nordbotten, J. M. (2014). Physics-based preconditioners for flow in fractured porous media. *Water Resources Research*, *50*, 1357–1373. <https://doi.org/10.1002/2012WR013034>
- Schwenck, N., Flemisch, B., Helmig, R., & Wohlmuth, B. I. (2015). Dimensionally reduced flow models in fractured porous media: Crossings and boundaries. *Computational Geosciences*, *19*(6), 1219–1230.
- Segall, P. (1985). Stress and subsidence resulting from subsurface fluid withdrawal in the epicentral region of the 1983 Coalinga earthquake. *Journal of Geophysical Research*, *90*(B8), 6801–6816.
- Segall, P., & Lu, S. (2015). Injection-induced seismicity: Poroelastic and earthquake nucleation effects. *Journal of Geophysical Research - Solid Earth*, *120*, 5082–5103. <https://doi.org/10.1002/2015JB012060>



- Segura, J. M., & Carol, I. (2004). On zero-thickness interface elements for diffusion problems. *International Journal for Numerical and Analytical Methods in Geomechanics*, 28(9), 947–962.
- Segura, J. M., & Carol, I. (2008a). Coupled HM analysis using zero-thickness interface elements with double nodes. Part I: Theoretical model. *International Journal for Numerical and Analytical Methods in Geomechanics*, 32(18), 2083–2101.
- Segura, J. M., & Carol, I. (2008b). Coupled HM analysis using zero-thickness interface elements with double nodes-Part II: Verification and application. *International Journal for Numerical and Analytical Methods in Geomechanics*, 32(18), 2103–2123.
- Shapiro, S. A., Huenges, E., & Borm, G. (1997). Estimating the crust permeability from fluid-injection-induced seismic emission at the KTB site. *Geophysical Journal International*, 131(2), F15–F18.
- Tecklenburg, J., Neuweiler, I., Carrera, J., & Dentz, M. (2016). Multi-rate mass transfer modeling of two-phase flow in highly heterogeneous fractured and porous media. *Advances in Water Resources*, 91, 63–77.
- Tunc, X., Faille, I., Gallouët, T., Cacas, M. C., & Havé, P. (2012). A model for conductive faults with non-matching grids. *Computational Geosciences*, 16(2), 277–296.
- Unsal, E., Matthäi, S. K., & Blunt, M. J. (2010). Simulation of multiphase flow in fractured reservoirs using a fracture-only model with transfer functions. *Computational Geosciences*, 14(4), 527–538.
- Vinci, C., Renner, J., & Steeb, H. (2014). A hybrid-dimensional approach for an efficient numerical modeling of the hydro-mechanics of fractures. *Water Resources Research*, 50, 1616–1635. <https://doi.org/10.1002/2013WR014154>
- Vujević, K., Graf, T., Simmons, C. T., & Werner, A. D. (2014). Impact of fracture network geometry on free convective flow patterns. *Advances in Water Resources*, 71, 65–80.
- Walsh, J. B. (1981). Effect of pore pressure and confining pressure on fracture permeability. *International Journal of Rock Mechanics and Mining Science and Geomechanics Abstracts*, 18(5), 429–435.
- Wang, R., & Kumpel, H. J. (2003). Poroelasticity: Efficient modeling of strongly coupled, slow deformation processes in a multilayered half-space. *Geophysics*, 68(2), 705–717.
- Warren, J. E., & Root, P. J. (1963). The behavior of naturally fractured reservoirs. *Society of Petroleum Engineers Journal*, 3(03), 245–255.
- White, J. A., & Borja, R. I. (2011). Block-preconditioned Newton-Krylov solvers for fully coupled flow and geomechanics. *Computational Geosciences*, 15(4), 647.
- White, J. A., Castelletto, N., & Tchelepi, H. A. (2016). Block-partitioned solvers for coupled poromechanics: A unified framework. *Computer Methods in Applied Mechanics and Engineering*, 303, 55–74.
- Witherspoon, P. A., Wang, J. S. Y., Iwai, K., & Gale, J. E. (1980). Validity of cubic law for fluid flow in a deformable rock fracture. *Water Resources Research*, 16(6), 1016–1024.
- Wu, Y. S., Liu, H. H., & Bodvarsson, G. S. (2004). A triple-continuum approach for modeling flow and transport processes in fractured rock. *Journal of Contaminant Hydrology*, 73(1), 145–179.
- Yao, J., Huang, Z., Li, Y., Wang, C., & Lv, X. (2010). Discrete fracture-vug network model for modeling fluid flow in fractured vuggy porous media. In International Oil and Gas Conference and Exhibition in China. Society of Petroleum Engineers.
- Zhang, N., Yao, J., Huang, Z., & Wang, Y. (2013). Accurate multiscale finite element method for numerical simulation of two-phase flow in fractured media using discrete-fracture model. *Journal of Computational Physics*, 242, 420–438.